






















Binary neutron star mergers using a discontinuous Galerkin-finite difference hybrid method

Nils Deppe^{1,2,3} , Francois Foucart⁴ , Marceline S. Bonilla⁷ ,
 Michael Boyle³ , Nicholas J. Corso^{5,3} , Matthew D. Duez⁹ ,
 Matthew Giesler³ , François Hébert⁶ , Lawrence
 E. Kidder³ , Yoonsoo Kim⁶ , Prayush Kumar⁸ , Isaac
 Legred⁶ , Geoffrey Lovelace⁷ , Elias R. Most⁶ , Jordan
 Moxon⁶ , Kyle C. Nelli⁶ , Harald P. Pfeiffer¹⁰ , Mark
 A. Scheel⁶ , Saul A. Teukolsky^{3,6} , William Throwe³ , and
 Nils L. Vu⁶ 

¹Department of Physics, Cornell University, Ithaca, New York 14853, USA

²Laboratory for Elementary Particle Physics, Cornell University, Ithaca, New York 14853, USA

³Cornell Center for Astrophysics and Planetary Science, Cornell University, Ithaca, New York 14853, USA

⁴Department of Physics & Astronomy, University of New Hampshire, Durham, New Hampshire 03824, USA

⁵Department of Astronomy, Cornell University, Ithaca, New York 14853, USA

⁶Theoretical Astrophysics 350-17, California Institute of Technology, Pasadena, CA 91125, USA

⁷Nicholas and Lee Begovich Center for Gravitational-Wave Physics and Astronomy, California State University Fullerton, Fullerton, CA 92834, USA

⁸International Centre for Theoretical Sciences, Tata Institute of Fundamental Research, Bangalore 560089, India

⁹Department of Physics & Astronomy, Washington State University, Pullman, Washington 99164, USA

¹⁰Max Planck Institute for Gravitational Physics (Albert Einstein Institute), D-14467 Potsdam, Germany

E-mail: nd357@cornell.edu

Abstract.

We present a discontinuous Galerkin-finite difference hybrid scheme that allows high-order shock capturing with the discontinuous Galerkin method for general relativistic magnetohydrodynamics in dynamical spacetimes. We present several optimizations and stability improvements to our algorithm that allow the hybrid method to successfully simulate single, rotating, and binary neutron stars. The hybrid method achieves the efficiency of discontinuous Galerkin methods throughout almost the entire spacetime during the inspiral phase, while being able to robustly capture shocks and resolve the stellar surfaces. We also use Cauchy-Characteristic evolution to compute the first gravitational waveforms at future null infinity from binary neutron star mergers. The simulations presented here are the first successful binary neutron star inspiral and merger simulations using discontinuous Galerkin methods.

Keywords: discontinuous Galerkin, Finite Difference, GRMHD, neutron star, binary neutron star, gravitational waves

Submitted to: *Class. Quantum Grav.*

1. Introduction

The discontinuous Galerkin (DG) method was first presented by Reed and Hill [1] to solve the neutron transport equation. Later, in a series of seminal papers, Cockburn and Shu applied the DG method to nonlinear hyperbolic conservation laws [2, 3, 4]. An important property of DG methods is that they guarantee linear stability in the L_2 norm for arbitrary high order [5, 6, 7]. While this means the DG method is very robust, DG alone is still subject to Godunov’s theorem [8]: at high order it produces oscillatory solutions. This means DG requires a nonlinear supplemental method for stability in the presence of discontinuities and large gradients. We extend the discontinuous Galerkin-finite difference (DG-FD) hybrid method developed in [9] to dynamical spacetimes. The method is implemented in the open-source numerical relativity code, **SpECTRE**[10].

Spectral-type methods have proven extremely useful in producing a large number of long and accurate gravitational waveforms from binary black hole merger simulations [11, 12, 13, 14, 15, 16, 17, 18, 19], as well as other applications in relativistic astrophysics [20, 21, 22, 23, 24, 25]. The Spectral Einstein Code (**SpEC**) [12] performs binary neutron star merger simulations by solving the spacetime using pseudospectral methods and the magnetohydrodynamics (MHD) using finite difference methods [26, 27, 28, 29, 30, 31, 32, 33]. However, these use completely separate grids requiring interpolation between them at every time/sub step. This interpolation adds non-trivial cost, though more importantly, **SpEC**’s use of large spectral elements causes significant load-imbalance and prohibitive cost as resolution is increased. This is because the spacetime is only two derivatives smoother than the MHD solution, and so the spectral approximation is less accurate at the stellar surfaces causing **SpEC**’s adaptive mesh refinement algorithm[19] to significantly increase the number of grid points in these regions. **SpEC** has leveraged its use of pseudospectral methods to produce relatively low-cost 10-15 orbits long simulations of binary neutron star (BNS) and black hole-neutron star (BHNS) [34, 35, 36] mergers with accuracy comparable to state-of-the art finite difference codes [37, 38, 39, 40]. Given its scaling issues when attempting higher resolution simulations, however, producing the longer, higher accuracy BNS and BHNS waveforms needed by next-generation gravitational wave detectors [41] with **SpEC** would be impractical. The same issues arise when attempting to capture the growth of magnetic fields due to MHD instabilities during and after merger, as well as the expected dynamo processes leading to the production of a large scale, organized magnetic field from the small scale field generated by these instabilities. Recent simulations have demonstrated the transfer of magnetic energy from small to large scales in merger simulations [42, 43, 44], yet even the highest resolution simulations available do not

show clear convergence of the magnetic field evolution during and after merger [45, 46]. The need to perform high-resolution MHD simulations is particularly acute given the importance of the large scale structure of the magnetic field on matter ejection and the electromagnetic signals powered by neutron star mergers [47, 48].

By using the same method (DG or finite difference) in each element for both the spacetime and MHD, **SpECTRE** is able to achieve robust convergence during the inspiral phase while avoiding the scaling issues limiting **SpEC**'s ability to perform high-resolution simulations. Recently, Ref. [49] successfully performed long-term simulations of static spacetimes using a DG-finite volume hybrid method to evolve the Einstein-Euler system. However, inspiral and merger simulations were not presented for black hole or neutron star binaries. There are several other next-generation numerical relativity codes using DG methods, including **bamps**[22, 50] and **Nmesh**[51]. Other next-generation codes like **GR-Athena++**[52, 53], **Athena-K**[54, 55, 56, 57], **Parthenon**[58], **GR-Chombo**[59], **Carpet-X**[60], **AsterX**[61], **GRAM-X**[62], and **Dendro-GR**[63, 64, 65] use FD methods (**Dendro-GR** combines this with wavelet-based adaptive mesh refinement) but are aimed at using Graphics Processing Units (GPUs). The code **SPHINCS BSSN**[66] uses smooth particle hydrodynamics to evolve the relativistic hydrodynamics and FD methods for the spacetime.

In this paper we present the improvements necessary for **SpECTRE** to simulate the inspiral and merger of a binary neutron star system using DG methods. We will present results of collapsing simulations in future work since several improvements to our algorithm currently in development will be necessary. In §2 we briefly review the generalized harmonic (GH) equations. In §3 we provide details about the improvements necessary since [9] to successfully simulate the inspiral and merger of two neutron stars. In §4 we present numerical results from simulations of a TOV star, rotating neutron star, and a binary neutron star merger, including the first gravitational waveforms extracted using Cauchy-Characteristic Evolution [67, 68, 69, 70, 71, 72, 73, 74, 75, 76, 77]. All simulations are done using the open-source code **SpECTRE** [78, 9, 10] using the scheme presented here. We conclude in §5.

2. Equations of Motion

We adopt the standard 3+1 form of the spacetime metric, (see, e.g., [79, 80]),

$$ds^2 = g_{ab}dx^a dx^b = -\alpha^2 dt^2 + \gamma_{ij} \left(dx^i + \beta^i dt\right) \left(dx^j + \beta^j dt\right), \quad (1)$$

where α is the lapse, β^i the shift vector, and γ_{ij} is the spatial metric. We use the Einstein summation convention, summing over repeated indices. Latin indices from the first part of the alphabet a, b, c, \dots denote spacetime indices ranging from 0 to 3, while Latin indices i, j, \dots are purely spatial, ranging from 1 to 3. We work in units where $c = G = M_\odot = 1$, and use geometrized Heaviside-Lorentz units where the magnetic field is rescaled by $1/\sqrt{4\pi}$ compared to Gaussian units.

We refer the reader to the literature [81, 82, 79] for a detailed description of the equations of general relativistic magnetohydrodynamics (GRMHD) and their

implementation in `SpECTRE`. The generalized harmonic (GH) equations are given by[83],

$$\partial_t g_{ab} = (1 + \gamma_1) \beta^k \partial_k g_{ab} - \alpha \Pi_{ab} - \gamma_1 \beta^i \Phi_{iab}, \quad (2)$$

$$\begin{aligned} \partial_t \Phi_{iab} &= \beta^k \partial_k \Phi_{iab} - \alpha \partial_i \Pi_{ab} + \alpha \gamma_2 \partial_i g_{ab} + \frac{1}{2} \alpha n^c n^d \Phi_{icd} \Pi_{ab} \\ &+ \alpha \gamma^{jk} n^c \Phi_{ijc} \Phi_{kab} - \alpha \gamma_2 \Phi_{iab}, \end{aligned} \quad (3)$$

$$\begin{aligned} \partial_t \Pi_{ab} &= \beta^k \partial_k \Pi_{ab} - \alpha \gamma^{ki} \partial_k \Phi_{iab} + \gamma_1 \gamma_2 \beta^k \partial_k g_{ab} \\ &+ 2\alpha g^{cd} \left(\gamma^{ij} \Phi_{ica} \Phi_{jdb} - \Pi_{ca} \Pi_{db} - g^{ef} \Gamma_{ace} \Gamma_{bdf} \right) \\ &- 2\alpha \nabla_{(a} H_{b)} - \frac{1}{2} \alpha n^c n^d \Pi_{cd} \Pi_{ab} - \alpha n^c \Pi_{ci} \gamma^{ij} \Phi_{jab} \\ &+ \alpha \gamma_0 \left(2\delta^c_{(a} n_{b)} - g_{ab} n^c \right) \mathcal{C}_c - \gamma_1 \gamma_2 \beta^i \Phi_{iab} \\ &- 16\pi \alpha \left(T_{ab} - \frac{1}{2} g_{ab} T^c_c \right), \end{aligned} \quad (4)$$

where g_{ab} is the spacetime metric, $\Phi_{iab} = \partial_i g_{ab}$, $\Pi_{ab} = n^c \partial_c g_{ab}$, n^a is the unit normal vector to the spatial slice, γ_0 damps the 1-index or gauge constraint $\mathcal{C}_a = H_a + \Gamma_a$, γ_1 controls the linear degeneracy of the system, γ_2 damps the 3-index constraint $\mathcal{C}_{iab} = \partial_i g_{ab} - \Phi_{iab}$, Γ_{abc} are the spacetime Christoffel symbols of the first kind, $\Gamma_a = g^{bc} \Gamma_{bca}$, and T_{ab} is the stress-energy tensor. The gauge source function H_a can be any arbitrary function depending only upon the spacetime coordinates x^a and g_{ab} (but not derivatives of g_{ab}). For the GRMHD system the trace-reversed stress-energy tensor that sources Π_{ab} is given by

$$T_{ab} - \frac{1}{2} g_{ab} T^c_c = (\rho h + b^2) u_a u_b + \left[\frac{1}{2} (\rho h + b^2) - p \right] g_{ab} - b_a b_b, \quad (5)$$

where u_a is the four-velocity of the fluid, ρ is the baryon rest mass density, p the fluid pressure, h the specific enthalpy, and $b^a = -\frac{1}{2} \epsilon^{abcd} F_{cd} u_b$ with $\epsilon_{abcd} = \sqrt{-g} [abcd]$, g the determinant of the spacetime metric and $[abcd] = \pm 1$ with $[0123] = +1$ is the flat-space antisymmetric symbol.

3. Discontinuous Galerkin-finite difference hybrid method in dynamical spacetimes

In this section we present our DG-FD hybrid method improvements necessary to simulate dynamical spacetimes. The reader is referred to [9] for the original algorithm and to [84] for improvements developed for simulating general relativistic force-free electrodynamics.

3.1. Generalized harmonic spectral filter

We use an exponential filter applied to the spectral coefficient c_i in order to reduce and eliminate aliasing-driven instabilities. Specifically, for a 1d spectral expansion

$$u(x) = \sum_{i=0}^N c_i P_i(x), \quad (6)$$

where $P_i(x)$ are the Legendre polynomials, we use the filter

$$c_i \rightarrow c_i \exp \left[-a \left(\frac{i}{N} \right)^{2b} \right]. \quad (7)$$

We choose the parameters $a = 36$ and $b = 64$ so that only the highest spectral mode is filtered. We only apply the filter to the GH variables g_{ab} , Φ_{iab} and Π_{ab} . Note that the filter drops the order of convergence for the GH variables from $\mathcal{O}(N + 1)$ to $\mathcal{O}(N)$ on the DG grid, but is necessary for stability.

3.2. Generalized harmonic finite difference method

When FD is necessary, we discretize the GH system using standard cell-centered central FD methods[‡]. In general, the order of accuracy of the FD derivatives for the GH system is two orders higher than that of the GRMHD system. That is, if we use second-order monotized central reconstruction [88], we use fourth-order FD derivatives of the GH system. We apply Kreiss-Oliger dissipation [89] as a filter to the GH variables before taking numerical derivatives and evaluating the time derivatives. Specifically, the filtered variable \tilde{u} is given by

$$\tilde{u}_i = u_i + \epsilon F^{(m)}(u_i), \quad (8)$$

for Kreiss-Oliger operator $F^{(m)}$ and $\epsilon \in [0, 1]$. The subscript \hat{i} refers to a grid point index. We use the filter $F^{(5)}$ when using fourth-order FD derivatives where $F^{(5)}$ is given by

$$F^{(5)}u_i = -\frac{375}{8} \left(\frac{1}{336}(u_{\hat{i}-2} + u_{\hat{i}+2}) - \frac{1}{84}(u_{\hat{i}-1} + u_{\hat{i}+1}) + \frac{1}{56}u_i \right). \quad (9)$$

The advantage of this approach is that the number of ghost zones (i.e., the number of grid points that are sent by neighboring elements to compute derivatives and perform reconstruction) is not increased for dissipation, and the GH system is still solved at a higher order than the GRMHD system.

We reconstruct the metric variables to subcell interfaces at the same order as the hydro variables. That is, if we use the fifth-order positivity-preserving adaptive-order (PPAO) scheme[90] to reconstruct the GRMHD variables, then we use unlimited fifth-order reconstruction for the metric.

3.3. GRMHD finite difference method

The overall method is very similar to that presented in [9, 90]. However, instead of reconstructing the pressure p we now reconstruct the “temperature” T of the fluid. This is because the temperature is an independent variable in equation of state tables, so even if there are numerical errors, as long as the temperature remains positive the reconstructed primitive state is “reasonable”.

[‡] See, e.g. [85, 86, 87] for a pedagogical overview.

3.4. Curved mesh finite difference method

SpECTRE solves hyperbolic systems of equations of the form

$$\partial_t u + \partial_i F^i(u) + B^i(u) \partial_i u = S(u), \quad (10)$$

where u are the evolved variables, $F^i(u)$ the fluxes, $B^i(u)$ non-conservative products, and $S(u)$ source terms. In our DG-FD method the computational domain is divided up into non-overlapping elements or cells, which we denote by Ω_k . This allows us to write the system (10) in semi-discrete form where time remains continuous. In the DG method one integrates the evolution equations (10) against spatial basis functions of degree N , which we denote by $\phi_{\check{i}}$. We index the basis functions and collocation points of the DG scheme with breve Latin indices, e.g. $\check{i}, \check{j}, \check{k}$. The basis functions are defined in the reference coordinates of each element, which we denote by $\xi^{\hat{i}} \in \{\xi, \eta, \zeta\}$. We use hatted indices to denote tensor components in the reference frame. The reference coordinates are mapped to the physical coordinates using the general function

$$x^i = x^i(\xi^{\hat{i}}, t). \quad (11)$$

Since the reference coordinates $\xi^{\hat{i}}$ are Cartesian, applying a FD scheme is comparatively straightforward to implement in the reference coordinates rather than the physical or inertial coordinates that the hyperbolic equations are written in.

In order to support FD on curved meshes SpECTRE now solves the equations in the form

$$\frac{\partial u}{\partial t} + \frac{1}{J} \partial_i \left[J \frac{\partial \xi^{\hat{i}}}{\partial x^i} (F^i - u v_g^i) \right] = S - u \partial_i v_g^i, \quad (12)$$

where v_g^i is the grid or mesh velocity and we can identify $F^i = J \frac{\partial \xi^{\hat{i}}}{\partial x^i} F^i$ as the ‘‘locally Cartesian flux’’ in the reference coordinates. This is analogous to how DG schemes are formulated [91, 9]. In practice we compute the mesh velocity divergence on the DG grid and project it to the FD grid. While this form is somewhat different from the strong form used by our DG solver, we can still rewrite the equations in a form that naturally hybridizes with a DG solver. In particular, the boundary corrections G in a DG scheme are essentially $n_i F^i$ where n_i is the normal covector to the spatial element interface and in the logical \hat{i} direction is given by

$$n_i^{(\hat{i})} = \frac{\partial \xi^{(\hat{i})}}{\partial x^i} \frac{1}{\sqrt{\frac{\partial \xi^{(\hat{i})}}{\partial x^j} \gamma^{jk} \frac{\partial \xi^{(\hat{i})}}{\partial x^k}}} = J \frac{\partial \xi^{(\hat{i})}}{\partial x^i} \frac{1}{\sqrt{J \frac{\partial \xi^{(\hat{i})}}{\partial x^j} \gamma^{jk} J \frac{\partial \xi^{(\hat{i})}}{\partial x^k}}}. \quad (13)$$

With $G^{(\hat{i})}$ as the boundary correction or numerical flux at the interface in direction \hat{i} , possibly including a high-order correction[92, 93], we can write the discretized FD evolution equation as

$$\begin{aligned} \frac{\partial u_{(\xi, \eta, \zeta)}}{\partial t} &= S_{(\xi, \eta, \zeta)} - u_{(\xi, \eta, \zeta)} \mathcal{P}(\partial_i v_g^i)_{(\xi, \eta, \zeta)} \\ &\quad - \frac{1}{J_{(\xi, \eta, \zeta)}} \left[\frac{(|n^{(\hat{\xi})}| G^{(\hat{\xi})})_{(\xi+1/2, \eta, \zeta)} - (|n^{(\hat{\xi})}| G^{(\hat{\xi})})_{(\xi-1/2, \eta, \zeta)}}{\Delta \xi} \right] \end{aligned}$$

$$\begin{aligned}
 & + \frac{\left(|n^{(\hat{\eta})}|G^{(\hat{\eta})}\right)_{(\xi,\eta+1/2,\zeta)} - \left(|n^{(\hat{\eta})}|G^{(\hat{\eta})}\right)_{(\xi,\eta-1/2,\zeta)}}{\Delta\eta} \\
 & + \frac{\left(|n^{(\hat{\zeta})}|G^{(\hat{\zeta})}\right)_{(\xi,\eta,\zeta+1/2)} - \left(|n^{(\hat{\zeta})}|G^{(\hat{\zeta})}\right)_{(\xi,\eta,\zeta-1/2)}}{\Delta\zeta} \Big], \quad (14)
 \end{aligned}$$

where \mathcal{P} is the projection operator from the DG to the FD grid as defined in [9] and $|n^{(i)}| = \sqrt{J \frac{\partial \xi^{(i)}}{\partial x^j} \gamma^{jk} J \frac{\partial \xi^{(i)}}{\partial x^k}}$ or $|n^{(i)}| = \sqrt{\frac{\partial \xi^{(i)}}{\partial x^j} \gamma^{jk} \frac{\partial \xi^{(i)}}{\partial x^k}}$ depending on which normal vector form is chosen. Since the correction $G^{(i)}$ is exactly what is used in a DG scheme we can straightforwardly hybridize the two schemes in a conservative manner, independent of the exact DG or FD formulation used. The primary reason for using the discretized form in Eq. 14 is for easier implementation on curved meshes since in this form the equations are simply the standard Cartesian evolution equations.

A non-trivial challenge on curved meshes is populating ghost zones. In **SpECTRE** we divide the computational domain into a set of conforming collections of elements called *blocks*. Each block has Cartesian block-logical coordinates $[-1, 1]^3$. These coordinates are then mapped by a possibly time-dependent map to the inertial frame in which the evolution equations are written. This is a standard approach in the spectral finite element method community and is similar to what **SpEC** uses [94, 17]. An example domain is a 2d disk made up of five deformed rectangles. One square is in the middle surrounded by 4 wedges. The specific challenge is reconstruction at block boundaries since the block-logical coordinates of two blocks in general do not align. This requires some form of interpolation to populate ghost points for the neighbor. Currently we use simple trilinear interpolation. However, we are developing an approach based on high-order limited interpolation inspired by [95].

In figure 1 we show an example of a 2d domain where the logical coordinates are not aligned. The left element must interpolate its solution to the red diamonds when populating the ghost zones for the right element. We currently use compact linear interpolation where neighbor points are not used during the interpolation. Not using neighbor points means that if the ghost zones lie outside the region enclosed by the grid points, extrapolation is used.

3.5. Troubled-cell indicators

One of the most important parts of the DG-FD hybrid method is the troubled-cell indicator (TCI) that determines when to switch from DG to FD and back. We still use the relaxed discrete maximum principle (RDMP) as discussed in [96, 9]. Specifically, the RDMP requires that

$$\min_{\mathcal{N}} [u(t^n)] - \delta \leq u^*(t^{n+1}) \leq \max_{\mathcal{N}} [u(t^n)] + \delta, \quad (15)$$

where \mathcal{N} are either the Neumann or Voronoi neighbors plus the element itself, δ is a parameter defined below that relaxes the discrete maximum principle, u are the conserved variables, and $u^*(t^{n+1})$ is a candidate solution at time t^{n+1} computed using

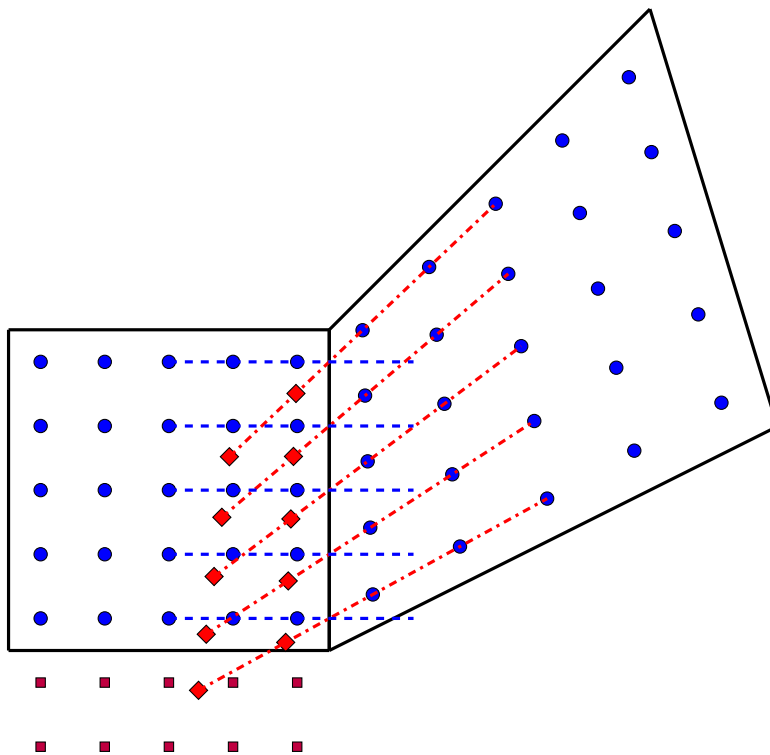


Figure 1. An illustration of the ghost points needed for the FD scheme where neighboring elements do not have aligned coordinate axes in their reference frames. Blue circles denote the cell-centered FD points in the two elements whose ghost cells are being exchanged, purple squares denote the cell-centered FD points in a neighboring element not used for ghost cell exchange in our current algorithm, and diamonds denote the ghost cells needed for reconstruction in the element on the right. The diagonal dash-dotted lines trace out lines of constant reference coordinates in the element on the right and dashed lines in the element on the left. Notice that the dashed and dash-dotted lines intersect on the element boundary.

an unlimited DG scheme. When computing $\max(u)$ and $\min(u)$ over an element using DG, we first project the DG solution to the FD grid and then compute the maximum and minimum over *both* the DG and FD grid. However, when an element is using FD we compute the maximum and minimum over the FD grid only. The maximum and minimum values of u^* are computed in the same manner as those of u . The parameter δ used to relax the discrete maximum principle is given by:

$$\delta = \max \left(\delta_0, \epsilon \left\{ \max_N [u(t^n)] - \min_N [u(t^n)] \right\} \right), \quad (16)$$

where, as in [96], we take $\delta_0 = 10^{-7}$ and $\epsilon = 10^{-3}$. If the condition 15 is satisfied, we say the variable u passes the RDMP.

We also continue to use the Persson indicator [97]; however, we have changed the details. Specifically, consider a variable u with a 1d spectral decomposition:

$$u(x) = \sum_{i=0}^N c_i P_i(x), \quad (17)$$

where in our case $P_i(x)$ are Legendre polynomials, and c_i are the spectral coefficients.

The Persson TCI essentially monitors the percentage of power in the highest spectral coefficient(s). To do this, we define \hat{u} as

$$\hat{u}(x) = c_N P_N(x). \quad (18)$$

and check that

$$(N+1)^\alpha \sqrt{\sum_{i=0}^N \hat{u}_i^2} > \sqrt{\sum_{i=0}^N u_i^2}, \quad (19)$$

where $(N+1)^\alpha$ can be precomputed and stored. We find that this mathematically equivalent condition to our previous check [9],

$$s^\Omega = \log_{10} \left(\sqrt{\frac{\sum_{i=0}^N \hat{u}_i^2}{\sum_{i=0}^N u_i^2}} \right) < s^e = -\alpha_N \log_{10}(N+1), \quad (20)$$

is cheaper and better behaved in the limit of $u \rightarrow 0$.

A significant change in handling initial data is that all elements start on the FD grid and then evaluate the TCI to see if restriction to the DG grid is allowed. This is particularly useful for initial data interpolated to the grid from another grid, e.g. when reading data from an elliptic solver such as [98, 99, 100, 101, 102]. The TCI used on the initial FD grid is essentially identical to the one used during the evolution described below, §3.5.2, except for the RDMP TCI. For the RDMP TCI the candidate solution is the restricted DG solution of the initial data.

Below we denote time levels by superscripts. For example, u^n is the value of the variable u at time t^n while u^{n+1} is the value of the variable u at time t^{n+1} . We also monitor several conserved magnetohydrodynamical variables, which are defined as

$$\begin{pmatrix} \tilde{D} \\ \tilde{S}_i \\ \tilde{\tau} \\ \tilde{B}^i \end{pmatrix} = \sqrt{\gamma} \begin{pmatrix} \rho W \\ (\rho h + b^2) W^2 v_i - \alpha b^0 b_i \\ (\rho h + b^2) *W^2 - \left[p + \frac{b^2}{2} \right] - (\alpha b^0)^2 - \rho W \\ B^i \end{pmatrix}, \quad (21)$$

where γ is the determinant of the spatial metric γ_{ij} , v^i is the spatial velocity of the fluid as measured by an observer at rest in the spatial hypersurfaces (“Eulerian observer”) is

$$v^i = \frac{1}{\alpha} \left(\frac{u^i}{u^0} + \beta^i \right), \quad (22)$$

with a corresponding Lorentz factor W

$$W = -u^a n_a = \alpha u^0 = \frac{1}{\sqrt{1 - \gamma_{ij} v^i v^j}} = \sqrt{1 + \gamma^{ij} u_i u_j}, \quad (23)$$

and

$$B^i = *F^{ia} n_a = \alpha *F^{0i}. \quad (24)$$

3.5.1. *TCI on DG grid for GRMHD* On the DG grid we require:

- (i) that $\min(\tilde{D}^{n+1})/\text{avg}(\sqrt{\gamma^n}) \geq D_{\min}$ on both the DG and the projected FD grid.
- (ii) that $\min(\tilde{\tau}^{n+1})/\text{avg}(\sqrt{\gamma^n}) \geq \tau_{\min}$ on both the DG and the projected FD grid.
- (iii) that $\max(\rho^{n+1})/\text{avg}(\sqrt{\gamma^n}) \geq \rho_{\text{atm}}$ on the DG grid. This is to ensure that we only apply the below TCI checks when the solution will not be reset to atmosphere since we would like to always use the DG solver in atmosphere.
- (iv) that $\tilde{B}^2 \leq 1.0 - \epsilon_B 2\tilde{\tau}\sqrt{\gamma}$ at all grid points in the DG element.
- (v) that primitive recovery is successful.
- (vi) if we are in atmosphere we mark the solution as admissible.
- (vii) that \tilde{D} and the pressure p pass the Persson TCI.
- (viii) that if $\max\left(\sqrt{\tilde{B}^i \delta_{ij} \tilde{B}^j}\right)$ is above a user-specified threshold, $\sqrt{\tilde{B}^i \delta_{ij} \tilde{B}^j}$ satisfies the Persson TCI.
- (ix) that the RDMP TCI passes for \tilde{D} , $\tilde{\tau}$, and $\sqrt{\tilde{B}^2}$.

If all requirements are met, then the DG solution is admissible. We use $\text{avg}(\sqrt{\gamma^n})$ to reduce computational cost since we can use the same average on both the DG and FD grid. This eliminates the need to project $\sqrt{\gamma}$ and also reduces the amount of memory bandwidth needed.

3.5.2. *TCI on FD grid for GRMHD* In order to switch to DG from FD, we require:

- (i) that $\min(\tilde{D}^{n+1})/\text{avg}(\sqrt{\gamma^n}) \geq D_{\min}$ and $\min(\tilde{\tau}^{n+1})/\text{avg}(\sqrt{\gamma^n}) \geq \tau_{\min}$ on the DG grid.
- (ii) that we did not need to fix the conservative variables (see §III.F of [103]) if we are not in atmosphere.
- (iii) that \tilde{D} and the pressure p pass the Persson TCI if we are not in atmosphere.
- (iv) that the RDMP TCI passes for \tilde{D} , $\tilde{\tau}$, and $\sqrt{\tilde{B}^2}$.
- (v) that if $\max\left(\sqrt{\tilde{B}^i \delta_{ij} \tilde{B}^j}\right)$ is above a user-specified threshold, $\sqrt{\tilde{B}^i \delta_{ij} \tilde{B}^j}$ satisfies the Persson TCI.

If all the above checks are satisfied, then the numerical solution is representable on the DG grid.

3.6. Restriction from FD to DG

The restriction operator $\mathcal{R}\S$ that interpolates variables from the FD to the DG grid, as presented in [9], is a 3d operator in 3 spatial dimensions. This means it is a matrix of size $(N + 1)^3 \times (2N + 1)^3$, resulting in a rather expensive matrix multiplication in the

§ referred to as reconstruction in [9], which we find is easily confused with the reconstruction done on the FD grid

|| N is the degree of the DG basis and $N + 1$ is the number of DG grid points per dimension.

troubled-cell indicator (TCI) used on the FD grid, where we restrict \tilde{D} , p , and optionally $\sqrt{B^i \delta_{ij} B^j}$ from the FD grid to the DG grid. This turns out to be a non-negligible expense and so instead we apply the 1d restriction operator dimension-by-dimension. This is a stronger constraint on the DG solution than the 3d restriction, but in addition to the reduced cost it also guarantees that if the solution is constant along an axis of the element on the FD grid, it will also be constant on the DG grid. This ultimately helps reduce noise introduced through restriction.

An additional two performance improvements that reduce how frequently the TCI is run on the FD grid were introduced after many of the simulations presented here were already completed. These are:

- (i) When an element switches from DG to FD, enough time must elapse for the discontinuous feature to propagate through the troubled element before a TCI check is necessary. A heuristic for choosing the number of time steps to wait before running the TCI on the FD grid is

$$\frac{\min(\Delta x)}{\Delta t} (2N + 1) \quad (25)$$

where $\min(\Delta x)$ is the minimum grid spacing between FD points in the inertial frame, Δt is the time step size, and $(2N + 1)$ is the number of FD grid points per dimension in the element. For example, for a P_5 DG-FD method with $\min(\Delta x)/\Delta t \sim 2$, we should wait ~ 22 time steps before checking the TCI after switching from DG to FD.

- (ii) Instead of checking the TCI every step after the initial check, we check with a specified frequency that we typically choose to be $\sim (2N - 1)$ time steps, primarily to reduce the overhead of TCI calls. A heuristic argument for the frequency at which to check is not clear. Essentially, one wants to minimize the overhead incurred by calls to the TCI while not spending too much time using FD when DG would work.

SpECTRE has input file options that allow controlling the two frequencies at which the TCI is applied on the FD grid.

A third option added to the TCI, but not yet extensively tested, is requiring the TCI to mark the solution in an element as admissible multiple times before switching back to DG. The motivation for this is to provide additional time for the FD solver to smooth the solution and to prevent having to switch back to the FD grid soon after switching to DG.

All three of these methods were necessary when studying more dynamical systems like current sheets in general relativistic force-free electrodynamics [84] and so is not just a characteristic of GRMHD, but dynamical systems in general.

3.7. Generalized harmonic system at DG-FD interface

For systems in flux-conservative and flux-balanced form, stable methods for a DG-FD hybrid scheme have been developed [9, 103, 84, 104, 96, 105, 106, 107, 49].

These are all based on a weak form of the system of partial differential equations. However, since the GH system is not in flux-conservative form it is not as clear how to couple the DG and FD solver. While weak forms for non-conservative systems exist [108, 104, 109, 110, 111, 107, 49], these formulations are not developed for FD schemes. We opt for a simple approach. On the FD grid we use cell-centered FD stencils using the GH variables in the ghost zones as interpolated by the DG grid. On the DG grid we interpolate the GH variables on the FD grid to the interface using unlimited reconstruction and then use the DG boundary correction just as is done for flux-conservative systems. In practice we find this to be stable except when the hybrid solver rapidly switches back and forth between the DG and FD grids. However, we view that as an issue with the TCI and not with how we handle the DG-FD interface for non-conservative systems. The same behavior is observed in simulations of current sheets in general relativistic force-free electrodynamics [84] and the methods described at the end of §3.6 result in a robust TCI that does not exhibit such pathological behavior.

3.8. Outer boundary conditions

We impose constraint-preserving boundary conditions on the GH constraint variables[83], first-order Bayliss-Turkel-type[112] boundary conditions on the gauge degrees of freedom[113], and a no-incoming radiation boundary condition on the physical degrees of freedom[83]. The boundary conditions are imposed using the Bjørhus method[114, 83]. In the future we plan to use Cauchy-Characteristic Matching to impose more realistic boundary conditions on the incoming physical fields[115]. We impose outflow boundary conditions on the GRMHD variables, filling ghost zones reflected about the outer boundary. For the DG grid this means the primitive variables are simply copied from the interior interface to the exterior one. However, we adjust the spatial velocity. Specifically, for an outward-directed normal vector n_i at the grid points, if $n_i v^i \geq 0$ we use $v_{\text{ghost}}^i = v^i$ while if $n_i v^i < 0$ then we set $v_{\text{ghost}}^i = v^i - n^i (n_j v^j)$. These boundary conditions allow us to stably evolve single and binary neutron star spacetimes for long times, though our simulations are terminated before the matter reaches the outer boundary. Because SpECTRE's FD solver does not yet have the ability to handle refinement boundaries, matter within 4 code units of the boundary of the inner region (see § 4.2) is removed from the evolution (i.e. the density is set to our numerical floor).

A crucial future improvement will be better handling of the matter outflows in two key ways. First, we need to add mesh refinement support to the FD solver in order to track matter outflows. Second, we plan to add the ability to impose outflow boundary conditions on the matter fields inside the computational domain. That is, rather than enforcing outflow boundary conditions in the wavezone we impose them closer to the binary and do not evolve the GRMHD system farther out. This is so that a larger computational domain can be used to track the GW emission but we can ignore low-density outflows in the wavezone to reduce computational cost.

3.9. Constraint damping

One non-trivial challenge in evolving the first-order GH system is choosing constraint damping parameters that allow for stable long-term evolutions while minimally decreasing the accuracy of the solution. For single neutron star simulations we use

$$\gamma_0 = 0.12 \exp\left(-\frac{r^2}{7.884855^2}\right) + 0.01, \quad (26)$$

$$\gamma_1 = 0.999 \exp\left(-\frac{r^2}{30^2}\right) - 0.999, \quad (27)$$

$$\gamma_2 = 1.2 \exp\left(-\frac{r^2}{7.884855^2}\right) + 0.01, \quad (28)$$

where r is the coordinate radius $r = \sqrt{x^i \delta_{ij} x^j}$ with δ_{ij} the Kronecker delta symbol. For binary neutron star mergers we use

$$\begin{aligned} \gamma_i = & \gamma_{i,A} \exp\left[\frac{|x^j - x_A^j|^2}{w_A^2}\right] + \gamma_{i,B} \exp\left[\frac{|x^j - x_B^j|^2}{w_B^2}\right] \\ & + \gamma_{i,C} \exp\left[\frac{r^2}{w_C^2}\right] + \gamma_{i,D} \end{aligned} \quad (29)$$

where x^i is the grid-frame coordinates, $x_{A,B}^i$ are the locations of the centers of the neutron stars in the grid frame, and the other parameters are freely specifiable constant. For the three parameters $\gamma_{0,1,2}$ entering the GH equations, we use

$$\gamma_{0,A} = \gamma_{0,B} = \gamma_{0,C} = 0.06277857994; \quad \gamma_{0,D} = 0.01; \quad (30)$$

$$\gamma_{1,C} = 0.999; \quad \gamma_{1,A} = \gamma_{1,B} = 0; \quad \gamma_{1,D} = -0.999; \quad (31)$$

$$\gamma_{2,A} = \gamma_{2,B} = 0.94167869922; \quad \gamma_{2,C} = 0.19182343873; \quad \gamma_{2,D} = 0.01; \quad (32)$$

$$w_A = w_B = 7.884855; \quad w_C = 51.60996. \quad (33)$$

These choices are drawn from our experience running similar systems with SpEC where we use the below functional forms depending on the masses of the stars M_A and M_B in solar masses. For γ_0 we use

$$\gamma_{0,A} = \frac{0.09}{M_A}, \quad \gamma_{0,B} = \frac{0.09}{M_B}, \quad \gamma_{0,C} = \frac{0.18}{M_A + M_B}, \quad \gamma_{0,D} = 0.01. \quad (34)$$

For γ_1 we use

$$\gamma_{1,A} = 0, \quad \gamma_{1,B} = 0, \quad \gamma_{1,C} = 0.999, \quad \gamma_{1,D} = -0.999, \quad (35)$$

which makes the zero-speed constraint fields propagate radially outward at the outer boundary. For γ_2 we use

$$\gamma_{2,A} = \frac{1.35}{M_A}, \quad \gamma_{2,B} = \frac{1.35}{M_B}, \quad \gamma_{2,C} = \frac{0.55}{M_A + M_B}, \quad \gamma_{2,D} = 0.01. \quad (36)$$

Finally, the weights are given by

$$w_A = 5.5M_A, \quad w_B = 5.5M_B, \quad w_C = 18(M_A + M_B). \quad (37)$$

K	8			16			32		
P_i	P_5	P_6	P_7	P_5	P_6	P_7	P_5	P_6	P_7
Δx [m]	599	507	439	299	253	219	150	127	110

Table 1. Resolutions of the FD grid in the central cube corresponding to our chosen grid parameters for the single star runs. The star is located within this central cube, which consists of K^3 P_i elements.

4. Numerical results

We now present numerical results from single and binary neutron star simulations. We refer to an element using $(N + 1)^3$ DG points as a P_N element or as using a P_N scheme. The corresponding FD grid has $(2N + 1)^3$ FD grid points.

4.1. Single Star

We begin our numerical evaluation of **SpECTRE**'s DG-FD hybrid method by simulating several configurations of single stars in equilibrium in full 3d using the harmonic gauge $H_a = 0$. We use the Harten-Lax-van Leer (HLL) Riemann solver [116] on all elements. Time evolution is performed using a third-order Runge-Kutta method. In all tests, the domain consists of an inner cube covering the region $[-17.8, 17.8]^3$ with a transition layer to a spherical boundary at $r = 100$ and a surrounding spherical shell covering $r \in [100, 250]$. The transition layer and spherical shell are divided into 6 regions with 90° opening angles (i.e. a cubed sphere geometry). We vary the resolution across the scenarios, but by convention, the cube consists of K^3 elements, where we may have $K \in [8, 16, 32]$. Each region of the inner spherical shells consists of $(K/2)^3$ elements, and each region the outer shells consists of $(K/2)_r \times (K/4)_{\theta, \phi}^2$ elements. For each value of K , we may further vary the resolution by changing the number of basis functions used by each DG element. Specifically, we use P_5 through P_7 elements. This choice is uniform across the entire domain, except when $K = 32$, in which case the shells only use P_5 elements, even if the central cube uses P_6 or P_7 ones.

All single star simulations are evolved with a polytropic equation of state,

$$p(\rho) = \kappa \rho^\Gamma, \quad (38)$$

with the polytropic exponent $\Gamma = 2$, polytropic constant $\kappa = 100$.

The following subsections outline the various tests that were run adopting this setup.

4.1.1. TOV star In the case of a static, spherically symmetric star, we follow the procedures of [103, 9]. Namely, we construct a star using the Tolman-Oppenheimer-Volkoff (TOV) solution [117, 118]. The star's central density is $\rho_c = 1.28 \times 10^{-3}$, such that the total mass in this solution is $M = 1.4M_\odot$. For FD cells in these simulations, we use the monotonized central reconstruction method [88]. We use this case to provide

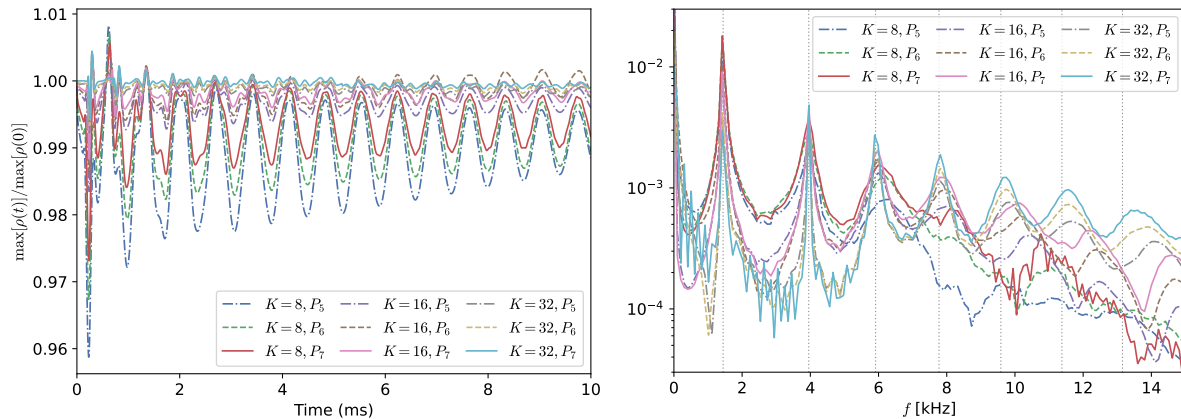


Figure 2. *Left:* Maximum value of the baryon rest mass density on the computational domain for all TOV star simulations, normalized to the maximum rest mass density at $t = 0$. *Right:* The power spectra of the maximum rest mass density for all the above cases. Vertical dashed lines correspond to the known dynamical spacetime frequencies for the system.

an in-depth exploration of the effects of resolution on our results. As such, we test all $K \in [8, 16, 32]$ and all DG basis functions P_5 through P_7 . In all cases, we run the simulation to $t = 10$ ms.

The left panel of figure 2 shows the evolution of the normalized maximum rest mass density over time. The $K = 8$ and $K = 16$ simulations use FD throughout the entire stellar interior, and although the $K = 32$ simulations use DG cells for at least part of the stellar interior, the P_5 and P_6 cases still use FD cells at the stellar core. This means that all simulations except for $K = 32, P_7$ will not have a grid point at the center and will have an offset in central density from the initial value. However, as the resolution improves, the density converges toward the initial value. The right panel of figure 2 shows the same data in the frequency domain, demonstrating that the oscillations in the data can largely be attributed to the known radial oscillation modes [119]. We find that even the lowest resolution simulation resolves two of the modes well, and as resolution improves, so does the quality and quantity of resolved modes.

4.1.2. Rotating neutron star To generate initial data for a uniformly rotating star, we numerically solve the Einstein-hydrostatic equilibrium equations according to the methods of [120, 121]. In our case, we generate a star of gravitational mass $M = 1.627M_\odot$ and rotational period 1.820 ms, such that the ratio of polar to equatorial radius is 0.85. We then load this initial data into SpECTRE and evolve the system. For FD cells in these simulations, we use the PPAO reconstruction method [90]. We test this scenario at two resolutions, $K \in [16, 32]$, both using the P_6 scheme, and we run both simulations to $t = 5$ ms.

As with the TOV case, figure 3 depicts the evolution of the maximum rest mass density over time. We see a decay in this maximum density over time, which is a

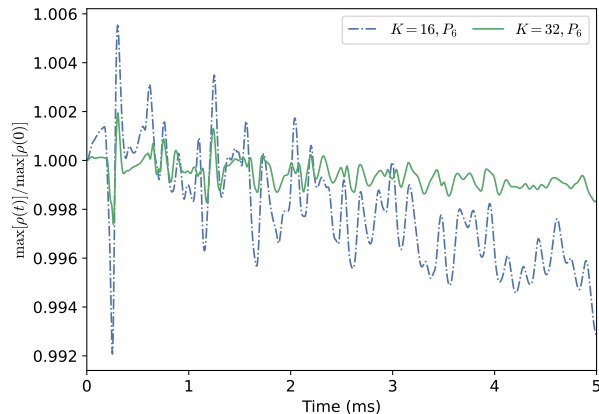


Figure 3. Maximum value of the baryon rest mass density on the computational domain for all Rotating star simulations, normalized to the maximum rest mass density at $t = 0$.

known consequence of the dissipative nature of FD schemes [9]. For the lower resolution $K = 16$ case, the decay is sub-percent level over our considered duration, and increasing the simulation resolution further reduces its effect.

4.2. Binary neutron star merger

4.2.1. Numerical setup To test **SpECTRE**'s ability to evolve binary neutron star (BNS) systems with the DG-FD hybrid method, we perform a series of BNS simulations with both **SpECTRE** and **SpEC**. For ease of comparison the simulations use the same initial conditions, gauge choice, and constraint damping parameter. Specifically, we consider an equal mass system with neutron stars of gravitational masses $M_A = M_B = 1.35M_\odot$. The stars have initial separation $d_0 = 47$ km in the coordinates of our initial data. The center of the neutron stars are initially at $x_A^i = (16, 0, 0)M_\odot$, $x_B^i = (-16, 0, 0)M_\odot$, with initial angular velocity $\Omega_0(M_A + M_B) = 0.0223$. The neutron stars have coordinate radii $R = 9.48$ (14 km).

We generate quasi-circular data with the **Spells** elliptic solver [98, 99, 100]. We use the simple ideal gas equation of state

$$p = \kappa\rho^\Gamma + \rho T = \kappa\rho^\Gamma + \rho(\Gamma - 1) \left(\epsilon - \frac{K\rho^{\Gamma-1}}{\Gamma - 1} \right), \quad (39)$$

$$T = (\Gamma - 1) \left(\epsilon - \frac{K\rho^{\Gamma-1}}{\Gamma - 1} \right), \quad (40)$$

$$\epsilon = \frac{1}{(\Gamma - 1)} \frac{p}{\rho} \quad (41)$$

with p the pressure, ρ the baryon density, ϵ the specific internal energy, and T a “temperature” variable effectively parametrizing the thermal energy of the fluid. We use $\Gamma = 2$ and $\kappa = 123.6$. All evolutions are performed using the harmonic gauge $H_a = 0$.

Besides these choices, the **SpEC** and **SpECTRE** simulations use very different numerical methods. The **SpEC** simulations use the standard setup described in [27, 122,

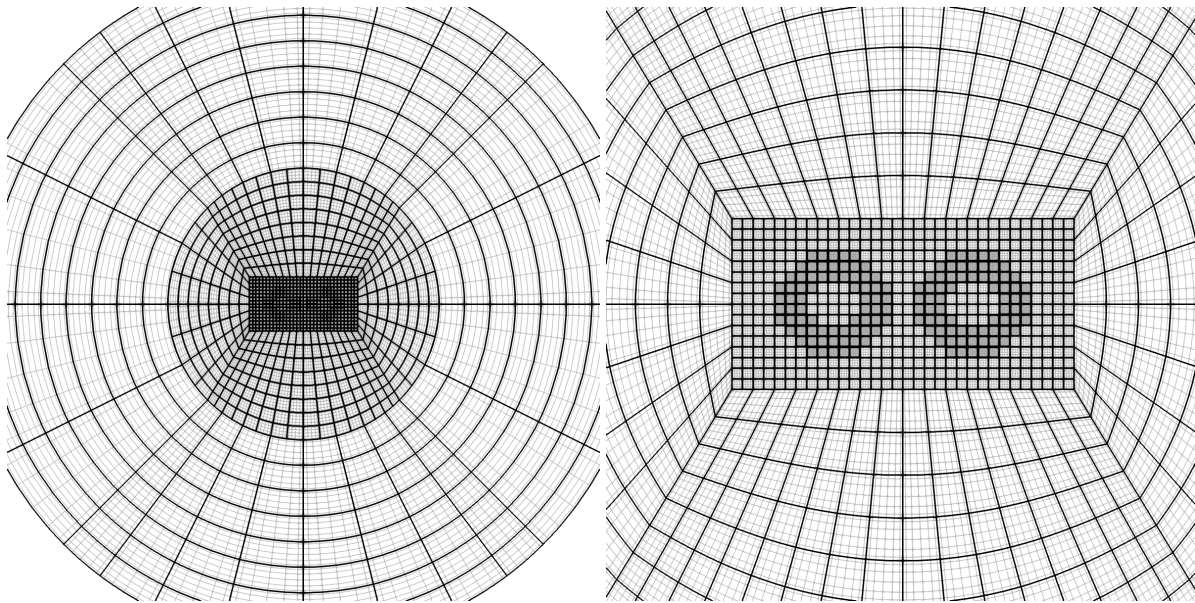


Figure 4. *Left:* Domain decomposition for the SpECTRE simulations. The central rectangle covers the two orbiting neutron stars, while curved elements extend from that box into the wave zone. Black lines denote element boundaries while intersections of grey lines are the grid point locations. *Right:* A zoom in on the central rectangle. FD is used in the circular regions with denser grey lines, which tracks the stellar surfaces. Note that which elements use FD or DG changes dynamically during simulations based on our troubled-cell indicator (TCI).

100], i.e. a pseudospectral grid for the evolution of the GH equations made of a small number of large subdomains adapted to the geometry of the system (78 pseudospectral subdomains during inspiral, including spheres close to the compact objects and in the wave zone, distorted cylinders and blocks in between), finite volume evolution of the hydrodynamics equations in the Valencia formalism [81] with fifth-order weighted essentially non-oscillatory (WENO5) [123, 124, 125] reconstruction from cell centers to cell faces and an HLL [116] approximate Riemann solver to calculate numerical fluxes on those faces. The finite difference grid is itself split during inspiral into $\sim (400 - 700)$ elements, with the number of elements changing over time as matter covers an increasingly large fraction of the pseudospectral grid. For the low-resolution SpEC simulation, each FD element uses 16^3 grid points excluding ghost zones and for the medium-resolution simulation each FD element uses 19^3 grid points excluding ghost zones. Ghost zones add 6 grid points per dimension for each simulation. Time evolution is performed using a third-order Runge-Kutta method. We run the SpEC simulations at 2 resolutions corresponding to our standard “low” and “medium” resolution settings ($\Delta x = [0.263, 0.211]M_\odot$ on the finite difference grid). In SpEC, the grid both rotates and contracts with the evolution of the neutron stars, in such a way as to keep the center of mass of each star fixed on the numerical grid.

SpECTRE on the other hand uses a larger number of smaller elements (14592 elements in total), making use of the mixed DG-FD algorithm described above. On FD elements,

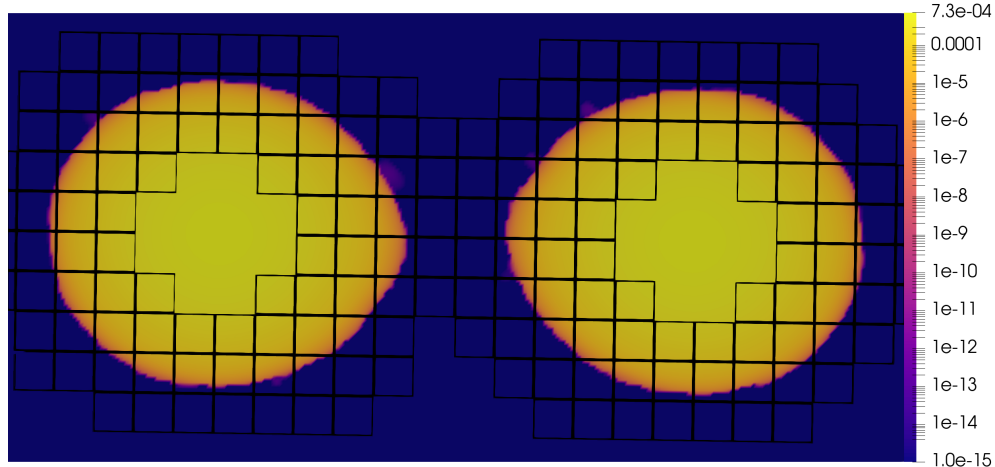


Figure 5. Baryon rest mass density at about $t = 3.5$ ms from the P_6 SpECTRE simulation. The elements outlined in black use FD. We see that during inspiral SpECTRE uses FD methods close to the stellar surfaces, and DG methods elsewhere.

we use the PPAO reconstruction method [90] and HLL Riemann solver. Time evolution is performed using a third-order Adams-Bashforth method [126]. We show the SpECTRE domain decomposition in figure 4. The inner part of the domain is constructed from a grid of $32 \times 16 \times 16$ cubes covering the region $[-40, 40] \times [-20, 20] \times [-20, 20]$ around the neutron stars. The outer part of the domain is a shell covering radii $r \in [100, 250]$, divided into 6 regions with 90° opening angles (“JuggleBalls” geometry). Each of these regions is divided into $8 \times 4 \times 4$ cubes (8 in the radial direction). Finally, the inner and outer region are connected by an envelope of 10 distorted cubes, each divided into $8 \times 8 \times 8$ elements. We vary resolution by changing the number of basis functions used by each DG elements. Specifically, we use P_4 through P_7 elements. Around the neutron stars, and when using FD, our effective grid resolution is thus $\Delta x = [0.278, 0.227, 0.192, 0.167]$. Practically, our experimentation with a range of different domain decompositions indicate that for P_4 , our errors are dominated by inaccurate evolution of the GH equations in the envelope and outer region. This is not surprising given the GH solver is running at only fourth order in this case. We will see that we observe a significant decrease in numerical error for e.g., the trajectories of the neutron stars, between P_4 and P_5 . In SpECTRE, the computational domain rotates with the neutron stars, but we do not perform any rescaling, i.e. the center of mass of the two neutron stars remains along the x -axis in grid coordinates, but the stars approach each other on that axis over the course of the evolution. In figure 5 we plot the baryon rest mass density at $t \approx 3.5$ ms. The elements outlined in black use FD. We see that during inspiral SpECTRE uses FD methods close to the stellar surfaces and DG methods elsewhere. During the merger itself, larger fractions of the computational domain switch to FD; how to optimize when to switch between FD and DG methods during the post-merger phase remains an open question.

SpEC and SpECTRE use the same mechanism to “correct” the evolved variables in

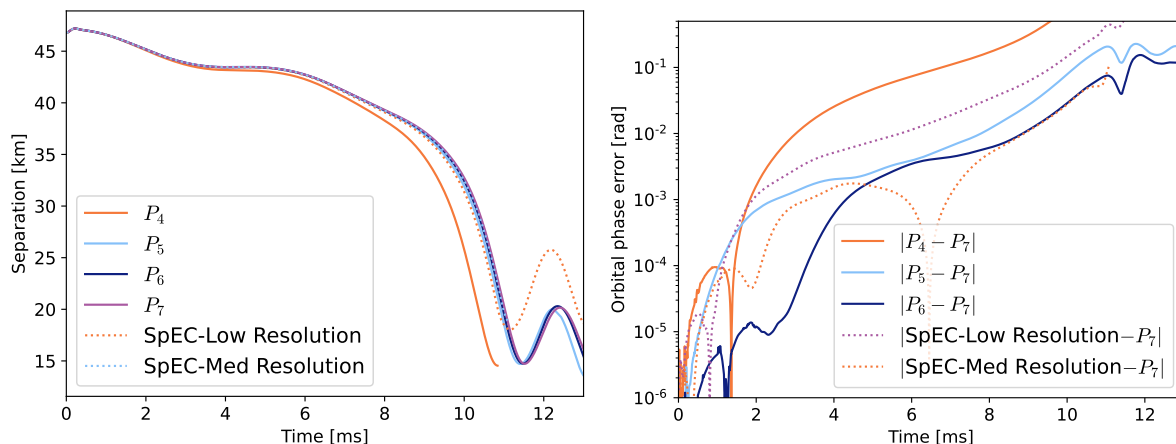


Figure 6. *Left:* Binary separation as a function of time for all six simulations (the MR SpEC simulation largely tracks the $N = 7$ SpECTRE simulation). *Right:* Difference in orbital phase with respect to the highest resolution SpECTRE simulation, for the $N = 6, 7$ SpECTRE simulations and the two SpEC simulations.

low-density regions [122, 127]. While SpEC additionally corrects the primitive variables (temperature, velocity) at densities $\rho < 2 \times 10^{-11}$ (i.e. roughly 8 orders of magnitude below the central density of the neutron star), SpECTRE only sets velocities to small ($< 10^{-4}$) values at $\rho < 9 \times 10^{-15}$, and does not correct the temperature. SpEC uses a density floor of $\rho = 10^{-13}$, while SpECTRE uses a floor of $\rho = 10^{-15}$.

4.2.2. Results Each neutron star goes through about 3.5 orbits before merger, on slightly eccentric orbits. Figure 6 provide us with more information about the numerical accuracy of the simulations. In the left panel, we show the binary separation as a function of time for all simulations. As previously mentioned, the P_4 SpECTRE simulation is significantly less accurate than all other simulations, likely because of the low-order methods used in the envelope. Experimentally we found that the P_4 scheme is fairly sensitive to the choice of domain decomposition in the outer regions. The P_5 through P_7 SpECTRE simulations show clear convergence of the merger time, with the SpEC and SpECTRE simulations agreeing within estimated numerical error. In the right panel we show the phase error, estimated here as the orbital phase difference with the P_7 SpECTRE simulation. The simulations show both the SpEC and SpECTRE simulations quickly approaching the results of the high-resolution SpECTRE simulations as resolution increases. We note that the trajectory and phase do not show clean pointwise convergence at all times, due to crossings in the trajectories at the time of periastron passage; i.e. around 4–5 ms. This is particularly visible in the phase difference for the SpECTRE simulations at time ~ 5 ms.

In figure 7, we show quantities that more directly track the error in the evolution of the GH and hydrodynamics equations. The left panel shows the violation of the gauge constraint, integrated over the entire computational domain. We see clear convergence with resolution before merger. At merger, we do not necessarily expect convergence as

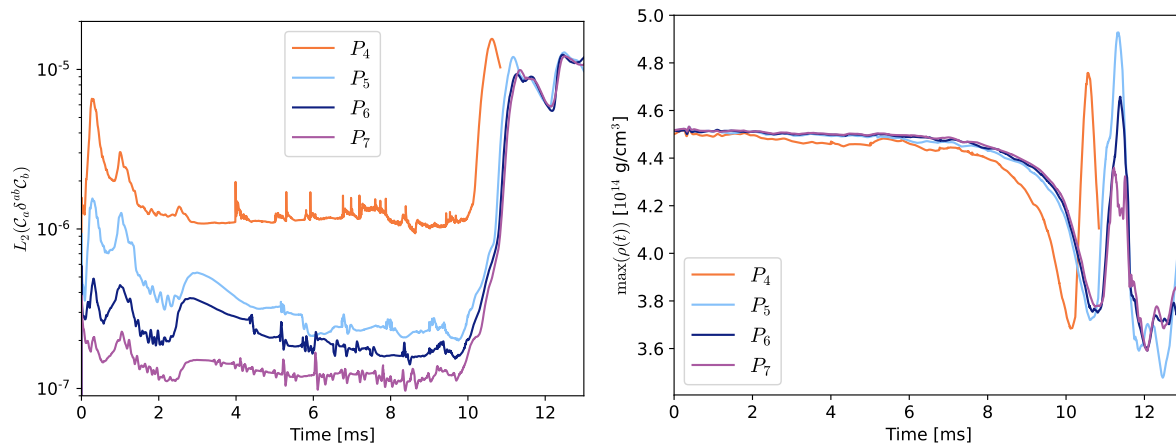


Figure 7. *Left:* Violation of the gauge constraint integrated over the computational domain, for all SpECTRE simulations. *Right:* Maximum value of the baryon density on the computational domain, for all SpECTRE simulations.

we introduce a fixed source of error at the boundary of the region where we allow matter to evolve. In the right panel we plot the maximum value of the baryon density on the computational domain. Errors in the evolution of the fluid equations typically lead to a slow decrease in the value of maximum density during inspiral—in addition to the physically expected decrease of the maximum density as each star is tidally distorted by its companion. We indeed see higher dissipation for P_4 , and convergence of the evolution of the maximum density for P_5, P_6, P_7 up to contact, at least in a time-averaged sense (i.e. ignoring the oscillations of the stars that do not remain exactly in phase at all resolutions, and lead to out-of-phase oscillations of the central density).

Finally, we show the first binary neutron star gravitational waveforms extracted using Cauchy-Characteristic Evolution (CCE) [67, 68, 69, 70, 71, 72, 73, 74, 75, 76, 77]. In figure 8 we plot the real part of the $(2, 2)$ mode of the strain h using an extraction worldtube located at $r = 200M$ at the three highest resolutions. We see convergence with increasing resolution of the Cauchy evolution. That is, the P_7 and P_6 simulations are closer together than the P_6 and P_5 simulations. A careful study of the convergence order and how it depends on different choices in the methods will be presented in a followup paper. The CCE discretization errors are negligible compared to the errors in Cauchy evolution. We evolve the CCE equations in spherical coordinates, with the evolved variables expanded radially using a Legendre-Gauss-Lobatto basis and spin-weighted spherical harmonics in the angular directions. The characteristic evolution uses a fifth-order Adams-Bashforth local time stepper [128] with an absolute error tolerance of 10^{-8} and a relative tolerance of 10^{-6} for the spin-weighted spherical harmonic variables and a relative error of 10^{-7} for the coordinate variables. We use $l_{\max} = 20$ for the expansion in spin-weighted spherical harmonics and filter out the top 2 modes. The radial grid uses 15 grid points and an exponential filter as in Eq. 7 with $a = 35$ and $b = 64$. The CCE data on the initial slice is determined using the conformal factor

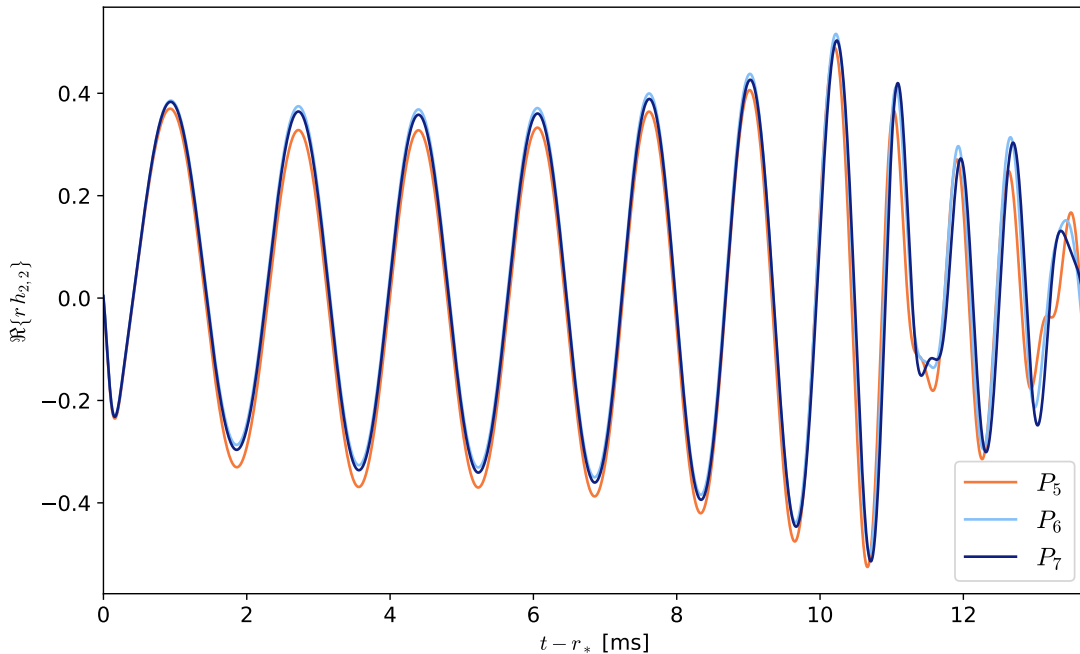


Figure 8. Shown is the real part the (2,2) of the strain rh for the binary merger simulation at three different resolutions. The waveform is extracted using SpECTRE’s Cauchy-Characteristic Evolution capabilities. Convergence with increasing resolution of the Cauchy evolution is observed. That is, the P_7 and P_6 simulations are closer together than the P_6 and P_5 simulations. A careful study of the convergence order and how it depends on different choices in the methods will be presented in a followup paper.

method [67, 68]. The CCE quantities like the strain, news, and Weyl scalars are output at \mathcal{I}^+ up to and including $l_{\max} = 8$. CCE also needs data on a worldtube from the Cauchy evolution as radial boundary conditions for the system. This data is kept at a resolution of $l_{\max} = 16$. We can ignore the effects of matter in our characteristic evolution because the extraction radius is in a region of atmosphere. That is, the effects of matter are neglected in CCE since none of the matter reaches the extraction radius. The effects of strongly gravitating matter near the extraction radii on the characteristic evolution have not been studied yet. We also perform a supertranslation using the `scri`[129, 130, 131, 132] and `sxs`[133] packages to set the strain to zero at retarded time zero. No time or phase alignment is done. While SpECTRE also outputs the news and all the Weyl scalars, we leave a careful analysis of CCE waveforms from BNS mergers as future work, pending a more detailed understanding of how various resolution, control system, extraction radii, and other choices affect the accuracy and convergence of the waveforms.

These simulations clearly demonstrate that the DG-FD hybrid scheme is capable of accurately evolving binary neutron star systems up to and through merger, as long as sufficiently high-order methods are used in the envelope and wave zone. Note that SpECTRE and SpEC have distinct (dis)advantages in the context of binary neutron star

evolutions. **SpEC** allows for very cost-effective evolutions of the binary thanks to spectral domains adapted to the geometry of the system. However, the use of a small number of large elements prevents **SpEC** from scaling beyond $\mathcal{O}(100)$ processors at low resolution. Additionally, attempting to go to higher resolution with **SpEC** leads to simulations whose cost is dominated by a few elements with large numbers of basis functions, typically situated around the surfaces of the stars. This would lead to extremely poor load-balancing, and has thus far limited our ability to perform higher resolution simulations. **SpECTRE**, on the other hand, is less cost-effective at low resolutions but can leverage a higher number of processors and, by using FD methods close to the surface of the star, is less sensitive to high-frequency noise in that region. In the simulations presented here, which use **SpEC** domains optimized over more than 10 years of experimentation but very unoptimized **SpECTRE** domain decompositions, the higher resolution **SpEC** simulation cost $14.2k$ CPU-hrs on the Wheeler cluster at Caltech to reach $t = 11$ ms. Wheeler has two 12-core Intel[®] Xeon[®] CPU E5-2680 v3 with a base clock of 2.50GHz CPUs per node. The P_5 **SpECTRE** simulation, with a FD grid spacing 5% coarser at the location of the neutron stars, costs $27.8k$ CPU-hrs, but used 288 cores instead of 120. The P_7 **SpECTRE** simulation used $117k$ CPU-hrs. This cost increase can be compared to the expected scaling for finite difference method (with cost $\propto \Delta x^{-4}$), which would predict a cost of $95k$ CPU-hrs for the P_7 simulation. Similarly, the P_6 simulation cost $52k$ CPU-hrs to reach the same time, while scaling as $\propto \Delta x^{-4}$ the P_6 cost predicts a cost of $54k$ CPU-hrs. These are already promising numbers that we expect will improve with better parallelization of the DG-FD hybrid algorithm. Specifically, we expect on-the-fly redistribution of elements to different processes (since FD elements are significantly more expensive than DG elements) and more optimized domain decompositions to significantly reduce the cost. Whether **SpECTRE** is able to outperform **SpEC**'s CPU time is currently unclear. However, one **SpECTRE**'s primary goals is to reduce wall time by scaling to more processors.

5. Conclusions

In this paper we gave a detailed description of our DG-FD hybrid method that can successfully solve challenging general relativistic astrophysics problems in dynamical spacetimes, including the simulation of a neutron star, a rotating neutron star, and a binary neutron star merger. Our method combines an unlimited DG solver with a conservative FD solver. Alternatively, this can be thought of as taking a standard FD code in numerical relativity and compressing the data to a DG grid wherever the solution is smooth. The DG solver is more efficient than the FD solver since no reconstruction is necessary and fewer Riemann problems need to be solved. The algorithm presented here is an extension of our previous work in static spacetimes [9]. The basic idea is that an unlimited DG solver is used wherever a troubled-cell indicator deems the DG solution admissible, while a FD solver is used elsewhere. Unlike classical limiting strategies like WENO [134, 135] which attempt to filter out unphysical oscillations, the

hybrid scheme prevents spurious oscillations from entering the solution. This is achieved by retaking any time step using a robust high-resolution shock-capturing conservative FD scheme where the DG solution was inadmissible, either because the DG scheme produced unphysical results like negative densities, or because a numerical criterion like the percentage of power in the highest modes deemed the DG solution bad. Our DG-FD hybrid scheme was used to perform the first simulations of a rotating neutron star and binary neutron star merger using DG methods. We show the first gravitational waveforms obtained from binary neutron star mergers using Cauchy-Characteristic Evolution [67, 68, 69, 70, 71, 72, 73, 74, 75, 76, 77], though leave a detailed analysis of the waveforms to future work¶. In the future we plan to improve our handling of curved meshes to allow tracking outflows in the post-merger phase, incorporate constrained transport for ensuring $\partial_i B^i = 0$ [136, 137, 138, 139, 140, 141, 142, 143, 144, 145, 146], use local adaptive time stepping using a linear multi-step method [128], use adaptive mesh refinement (e.g. [19, 147, 50]), dynamic continuous load-balancing, and an optimized domain decomposition.

Acknowledgments

Charm++/Converse [148] was developed by the Parallel Programming Laboratory in the Department of Computer Science at the University of Illinois at Urbana-Champaign. The figures in this article were produced with `matplotlib` [149, 150], `TikZ` [151] and `ParaView` [152, 153]. Computations were performed with the Wheeler cluster at Caltech and the mbot cluster at Cornell. This work was supported in part by the Sherman Fairchild Foundation and by NSF Grants No. PHY-2309211, No. PHY-2309231, and No. OAC-2209656 at Caltech, and NSF Grants No. PHY-2207342, No. PHY-2407742 and No. OAC-2209655 at Cornell. F.F. gratefully acknowledges support from the Department of Energy, Office of Science, Office of Nuclear Physics, under contract number DE-AC02-05CH11231, from NASA through grant 80NSSC22K0719, and from the NSF through grant AST-2107932. M.D. gratefully acknowledges support from the NSF through grant PHY-2110287 and support from NASA through grant 80NSSC22K0719. GL and MSB acknowledge support from NSF award PHY-2208014, the Dan Black Family Trust and Nicholas and Lee Begovich. I.L. acknowledges support from the Department of Energy under award number DE-SC0023101. ERM acknowledges support by the National Science Foundation under Grant No. AST-2307394 and PHY-2309210, the NSF Frontera supercomputer under grant AST21006, and Delta at the National Center for Supercomputing Applications (NCSA) through allocation PHY210074 from the Advanced Cyberinfrastructure Coordination Ecosystem: Services & Support (ACCESS) program, which is supported by National Science Foundation grants #2138259, #2138286, #2138307, #2137603, and #2138296. ERM further acknowledges support on Perlmutter through NERSC under grant m4575. P.K.

¶ Cauchy-Characteristic Evolution currently does not take the effects of matter passing through the worldtube into account and so long-term post merger wave extraction will require careful study.

acknowledges support of the Department of Atomic Energy, Government of India, under project no. RTI4001, and by the Ashok and Gita Vaish Early Career Faculty Fellowship at the International Centre for Theoretical Sciences.

References

- [1] William H Reed and TR Hill. Triangular mesh methods for the neutron transport equation. Technical report, Los Alamos Scientific Lab., N. Mex.(USA), 1973.
- [2] Bernardo Cockburn and Chi-Wang Shu. TVB Runge-Kutta local projection discontinuous Galerkin finite element method for conservation laws. II. General framework. *Mathematics of Computation*, 52(186):411–435, 1989.
- [3] Bernardo Cockburn, San-Yih Lin, and Chi-Wang Shu. TVB Runge-Kutta local projection discontinuous Galerkin finite element method for conservation laws III: One-dimensional systems. *Journal of Computational Physics*, 84(1):90 – 113, 1989.
- [4] B. Cockburn, S. Hou, and C.-W. Shu. The Runge-Kutta local projection discontinuous Galerkin finite element method for conservation laws. IV. The multidimensional case. *Mathematics of Computation*, 54:545–581, April 1990.
- [5] Guang Shan Jiang and Chi-Wang Shu. On a cell entropy inequality for discontinuous Galerkin methods. *Mathematics of Computation*, 62(206):531–538, 1994.
- [6] Timothy Barth, Pierre Charrier, and Nagi N Mansour. Energy stable flux formulas for the discontinuous Galerkin discretization of first order nonlinear conservation laws. Technical Report 20010095444, NASA Technical Reports Server, 2001.
- [7] Songming Hou and Xu-Dong Liu. Solutions of multi-dimensional hyperbolic systems of conservation laws by square entropy condition satisfying discontinuous Galerkin method. *Journal of Scientific Computing*, 31(1-2):127–151, 2007.
- [8] S. K. Godunov. A difference method for numerical calculation of discontinuous solutions of the equations of hydrodynamics. *Mat. Sb. (N.S.)*, 47(89):271–306, 1959.
- [9] Nils Deppe, François Hébert, Lawrence E. Kidder, and Saul A. Teukolsky. A high-order shock capturing discontinuous Galerkin–finite difference hybrid method for GRMHD. *Class. Quant. Grav.*, 39(19):195001, 2022.
- [10] Nils Deppe, William Throwe, Lawrence E. Kidder, Nils L. Vu, Kyle C. Nelli, Cristóbal Armaza, Marceline S. Bonilla, François Hébert, Yoonsoo Kim, Prayush Kumar, Geoffrey Lovelace, Alexandra Macedo, Jordan Moxon, Eamonn O’Shea, Harald P. Pfeiffer, Mark A. Scheel, Saul A. Teukolsky, Nikolas A. Wittek, et al. SpECTRE v2024.03.19. 10.5281/zenodo.10841324, 3 2024.
- [11] Michael Boyle et al. The SXS Collaboration catalog of binary black hole simulations. *Class. Quant. Grav.*, 36(19):195006, 2019.
- [12] <https://www.black-holes.org/SpEC.html>.
- [13] Mark A. Scheel, Michael Boyle, Tony Chu, Lawrence E. Kidder, Keith D. Matthews, and Harald P. Pfeiffer. High-accuracy waveforms for binary black hole inspiral, merger, and ringdown. *Phys. Rev. D*, 79:024003, 2009.
- [14] Bela Szilagyi, Lee Lindblom, and Mark A. Scheel. Simulations of Binary Black Hole Mergers Using Spectral Methods. *Phys. Rev. D*, 80:124010, 2009.
- [15] Geoffrey Lovelace, Mark. A. Scheel, and Bela Szilagyi. Simulating merging binary black holes with nearly extremal spins. *Phys. Rev. D*, 83:024010, 2011.
- [16] Luisa T. Buchman, Harald P. Pfeiffer, Mark A. Scheel, and Bela Szilagyi. Simulations of non-equal mass black hole binaries with spectral methods. *Phys. Rev. D*, 86:084033, 2012.
- [17] Daniel A. Hemberger, Mark A. Scheel, Lawrence E. Kidder, Béla Szilágyi, Geoffrey Lovelace, Nicholas W. Taylor, and Saul A. Teukolsky. Dynamical excision boundaries in spectral evolutions of binary black hole spacetimes. *Class. Quant. Grav.*, 30:115001, 2013.
- [18] Mark A. Scheel, Matthew Giesler, Daniel A. Hemberger, Geoffrey Lovelace, Kevin Kuper, Michael

- Boyle, B. Szilágyi, and Lawrence E. Kidder. Improved methods for simulating nearly extremal binary black holes. *Class. Quant. Grav.*, 32(10):105009, 2015.
- [19] Béla Szilágyi. Key Elements of Robustness in Binary Black Hole Evolutions using Spectral Methods. *Int. J. Mod. Phys. D*, 23(7):1430014, 2014.
- [20] S. Bonazzola, E. Gourgoulhon, and J. A. Marck. Spectral methods in general relativistic astrophysics. *J. Comput. Appl. Math.*, 109:433, 1999.
- [21] Claudio Meringolo and Sergio Servidio. Aliasing instabilities in the numerical evolution of the Einstein field equations. *Gen. Rel. Grav.*, 53(10):95, 2021.
- [22] David Hilditch, Andreas Weyhausen, and Bernd Brügmann. Pseudospectral method for gravitational wave collapse. *Phys. Rev. D*, 93(6):063006, 2016.
- [23] Alireza Rashti, Francesco Maria Fabbri, Bernd Brügmann, Swami Vivekanandji Chaurasia, Tim Dietrich, Maximiliano Ujevic, and Wolfgang Tichy. New pseudospectral code for the construction of initial data. *Phys. Rev. D*, 105(10):104027, 2022.
- [24] Claudio Meringolo, Sergio Servidio, and Pierluigi Veltri. A spectral method algorithm for numerical simulations of gravitational fields. *Class. Quant. Grav.*, 38(7):075027, 2021.
- [25] Wolfgang Tichy. Long term black hole evolution with the BSSN system by pseudo-spectral methods. *Phys. Rev. D*, 80:104034, 2009.
- [26] Matthew D. Duez, Lawrence E. Kidder, and Saul A. Teukolsky. Evolving relativistic fluid spacetimes using pseudospectral methods and finite differencing. In *11th Marcel Grossmann Meeting on General Relativity*, pages 1570–1572, 2 2007.
- [27] Matthew D. Duez, Francois Foucart, Lawrence E. Kidder, Harald P. Pfeiffer, Mark A. Scheel, and Saul A. Teukolsky. Evolving black hole-neutron star binaries in general relativity using pseudospectral and finite difference methods. *Phys.Rev.D*, 78(10):104015, November 2008.
- [28] Matthew D. Duez, Francois Foucart, Lawrence E. Kidder, Christian D. Ott, and Saul A. Teukolsky. Equation of state effects in black hole-neutron star mergers. *Class. Quant. Grav.*, 27:114106, 2010.
- [29] Francois Foucart, Matthew D. Duez, Lawrence E. Kidder, and Saul A. Teukolsky. Black hole-neutron star mergers: effects of the orientation of the black hole spin. *Phys. Rev. D*, 83:024005, 2011.
- [30] Curran D. Muhlberger, Fatemeh Hossein Nouri, Matthew D. Duez, Francois Foucart, Lawrence E. Kidder, Christian D. Ott, Mark A. Scheel, Béla Szilágyi, and Saul A. Teukolsky. Magnetic effects on the low-T/—W— instability in differentially rotating neutron stars. *Phys. Rev. D*, 90(10):104014, 2014.
- [31] Nick Tacik et al. Binary Neutron Stars with Arbitrary Spins in Numerical Relativity. *Phys. Rev. D*, 92(12):124012, 2015. [Erratum: Phys.Rev.D 94, 049903 (2016)].
- [32] Francois Foucart, Roland Haas, Matthew D. Duez, Evan O’Connor, Christian D. Ott, Luke Roberts, Lawrence E. Kidder, Jonas Lippuner, Harald P. Pfeiffer, and Mark A. Scheel. Low mass binary neutron star mergers : gravitational waves and neutrino emission. *Phys. Rev. D*, 93(4):044019, 2016.
- [33] Roland Haas et al. Simulations of inspiraling and merging double neutron stars using the Spectral Einstein Code. *Phys. Rev. D*, 93(12):124062, 2016.
- [34] Francois Foucart et al. Gravitational waveforms from spectral Einstein code simulations: Neutron star-neutron star and low-mass black hole-neutron star binaries. *Phys. Rev. D*, 99(4):044008, 2019.
- [35] Francois Foucart et al. High-accuracy waveforms for black hole-neutron star systems with spinning black holes. *Phys. Rev. D*, 103(6):064007, 2021.
- [36] Alexander Knight, Francois Foucart, Matthew D. Duez, Mike Boyle, Lawrence E. Kidder, Harald P. Pfeiffer, and Mark A. Scheel. Gravitational Waves from Binary Neutron Star Mergers with a Spectral Equation of State. 7 2023.
- [37] David Radice, Luciano Rezzolla, and Filippo Galeazzi. High-Order Numerical-Relativity Simulations of Binary Neutron Stars. *ASP Conf. Ser.*, 498:121–126, 2015.

- [38] Kenta Kiuchi, Kyohei Kawaguchi, Koutarou Kyutoku, Yuichiro Sekiguchi, Masaru Shibata, and Keisuke Taniguchi. Sub-radian-accuracy gravitational waveforms of coalescing binary neutron stars in numerical relativity. *Phys. Rev. D*, 96(8):084060, 2017.
- [39] Tim Dietrich, David Radice, Sebastiano Bernuzzi, Francesco Zappa, Albino Perego, Bernd Brügmann, Swami Vivekanandji Chaurasia, Reetika Dudi, Wolfgang Tichy, and Maximiliano Ujevic. CoRe database of binary neutron star merger waveforms. *Class. Quant. Grav.*, 35(24):24LT01, 2018.
- [40] Alejandra Gonzalez et al. Second release of the CoRe database of binary neutron star merger waveforms. *Class. Quant. Grav.*, 40(8):085011, 2023.
- [41] Michael Pürrer and Carl-Johan Haster. Gravitational waveform accuracy requirements for future ground-based detectors. *Phys. Rev. Res.*, 2:023151, May 2020.
- [42] Ricard Aguilera-Miret, Carlos Palenzuela, Federico Carrasco, and Daniele Viganò. Role of turbulence and winding in the development of large-scale, strong magnetic fields in long-lived remnants of binary neutron star mergers. *Phys. Rev. D*, 108(10):103001, 2023.
- [43] Kenta Kiuchi, Alexis Reboul-Salze, Masaru Shibata, and Yuichiro Sekiguchi. A large-scale magnetic field produced by a solar-like dynamo in binary neutron star mergers. *Nature Astron.*, 8(3):298–307, 2024.
- [44] Luciano Combi and Daniel M. Siegel. Jets from Neutron-Star Merger Remnants and Massive Blue Kilonovae. *Phys. Rev. Lett.*, 131(23):231402, 2023.
- [45] Kenta Kiuchi, Pablo Cerdá-Durán, Koutarou Kyutoku, Yuichiro Sekiguchi, and Masaru Shibata. Efficient magnetic-field amplification due to the Kelvin-Helmholtz instability in binary neutron star mergers. *Phys. Rev. D*, 92(12):124034, 2015.
- [46] Carlos Palenzuela, Steven Liebling, and Borja Miñano. Large eddy simulations of magnetized mergers of neutron stars with neutrinos. *Phys. Rev. D*, 105(10):103020, 2022.
- [47] I. M. Christie, A. Lalakos, A. Tchekhovskoy, R. Fernández, F. Foucart, E. Quataert, and D. Kasen. The Role of Magnetic Field Geometry in the Evolution of Neutron Star Merger Accretion Discs. *Mon. Not. Roy. Astron. Soc.*, 490(4):4811–4825, 2019.
- [48] Sebastiaan de Haas, Pablo Bosch, Philipp Mösta, Sanjana Curtis, and Nathanyel Schut. Magnetic field effects on nucleosynthesis and kilonovae from neutron star merger remnants. *Mon. Not. Roy. Astron. Soc.*, 527(2):2240–2250, 2023.
- [49] Michael Dumbser, Olindo Zanotti, Elena Gaburro, and Ilya Peshkov. A well-balanced discontinuous Galerkin method for the first-order Z4 formulation of the Einstein–Euler system. *J. Comput. Phys.*, 504:112875, 2024.
- [50] Sarah Renkhoff, Daniela Cors, David Hilditch, and Bernd Brügmann. Adaptive hp refinement for spectral elements in numerical relativity. *Phys. Rev. D*, 107(10):104043, 2023.
- [51] Wolfgang Tichy, Liwei Ji, Ananya Adhikari, Alireza Rashti, and Michal Pirog. The new discontinuous Galerkin methods based numerical relativity program Nmesh. *Class. Quant. Grav.*, 40(2):025004, 2023.
- [52] William Cook, Boris Daszuta, Jacob Fields, Peter Hammond, Simone Albanesi, Francesco Zappa, Sebastiano Bernuzzi, and David Radice. GR-Athena++: General-relativistic magnetohydrodynamics simulations of neutron star spacetimes. 11 2023.
- [53] Boris Daszuta and William Cook. GR-Athena++: magnetohydrodynamical evolution with dynamical space-time. 6 2024.
- [54] James M. Stone et al. Athena-k. <https://gitlab.com/theias/hpc/jmstone/athena-parthenon/athenak>, 2024.
- [55] James M. Stone, Patrick D. Mullen, Drummond Fielding, Philipp Grete, Minghao Guo, Philipp Kempster, Elias R. Most, Christopher J. White, and George N. Wong. AthenaK: A Performance-Portable Version of the Athena++ AMR Framework. *arXiv e-prints*, page arXiv:2409.16053, September 2024.
- [56] Hengrui Zhu, Jacob Fields, Francesco Zappa, David Radice, James Stone, Alireza Rashti, William Cook, Sebastiano Bernuzzi, and Boris Daszuta. Performance-Portable Numerical Relativity

- with AthenaK. 9 2024.
- [57] Jacob Fields, Hengrui Zhu, David Radice, James M. Stone, William Cook, Sebastiano Bernuzzi, and Boris Daszuta. Performance-Portable Binary Neutron Star Mergers with AthenaK. 9 2024.
- [58] Joshua Dolence et al. Parthenon. <https://github.com/parthenon-hpc-lab/parthenon>, 2024.
- [59] Katy Clough, Pau Figueras, Hal Finkel, Markus Kunesch, Eugene A. Lim, and Saran Tunyasuvunakool. GRChombo : Numerical Relativity with Adaptive Mesh Refinement. *Class. Quant. Grav.*, 32(24):245011, 2015.
- [60] Erik Schnetter et al. Carpetx. <https://github.com/eschnett/CarpetX>, 2024.
- [61] Jay Kalinani, Steven Brandt, Manuela Campanelli, Riccardo Ciolfi, Lorenzo Ennoggi, Bruno Giacomazzo, Roland Haas, Liwei Ji, Federico Lopez Armengol, Erik Schnetter, and Yosef Zlochower. AsterX: a new open-source GPU-accelerated GRMHD code for dynamical spacetimes. In *APS April Meeting Abstracts*, volume 2023 of *APS Meeting Abstracts*, page F08.008, January 2023.
- [62] Swapnil Shankar, Philipp Mösta, Steven R. Brandt, Roland Haas, Erik Schnetter, and Yannick de Graaf. GRaM-X: a new GPU-accelerated dynamical spacetime GRMHD code for Exascale computing with the Einstein Toolkit. *Class. Quant. Grav.*, 40(20):205009, 2023.
- [63] Milinda Fernando, David Neilsen, Eric Hirschmann, Yosef Zlochower, Hari Sundar, Omar Ghattas, and George Biros. A gpu-accelerated amr solver for gravitational wave propagation. In *SC22: International Conference for High Performance Computing, Networking, Storage and Analysis*, pages 1–15, 2022.
- [64] Milinda Fernando, David Neilsen, Hyun Lim, Eric Hirschmann, and Hari Sundar. Massively Parallel Simulations of Binary Black Hole Intermediate-Mass-Ratio Inspirals. *SIAM J. Sci. Comput.*, 41(2):C97–C138, 2019.
- [65] Milinda Fernando, David Neilsen, Yosef Zlochower, Eric W. Hirschmann, and Hari Sundar. Massively parallel simulations of binary black holes with adaptive wavelet multiresolution. *Phys. Rev. D*, 107(6):064035, 2023.
- [66] Peter Diener, Stephan Rosswog, and Francesco Torsello. Simulating neutron star mergers with the Lagrangian Numerical Relativity code SPHINCS_BSSN. *Eur. Phys. J. A*, 58(4):74, 2022.
- [67] Jordan Moxon, Mark A. Scheel, and Saul A. Teukolsky. Improved Cauchy-characteristic evolution system for high-precision numerical relativity waveforms. *Phys. Rev. D*, 102(4):044052, August 2020.
- [68] Jordan Moxon, Mark A. Scheel, Saul A. Teukolsky, Nils Deppe, Nils Fischer, Francois Hébert, Lawrence E. Kidder, and William Throwe. SpECTRE Cauchy-characteristic evolution system for rapid, precise waveform extraction. *Phys. Rev. D*, 107(6):064013, 2023.
- [69] Nigel T. Bishop, Roberto Gómez, Luis Lehner, and Jeffrey Winicour. Cauchy-characteristic extraction in numerical relativity. *Phys. Rev. D*, 54(10):6153–6165, November 1996.
- [70] Nigel T. Bishop, Roberto Gomez, Luis Lehner, Bela Szilagyi, Jeffrey Winicour, and Richard A. Isaacson. Cauchy-Characteristic Matching. In Bala R. Iyer and Biplab Bhawal, editors, *Black Holes, Gravitational Radiation, and the Universe: Essays in Honor of C.V. Vishveshwara*, page 383, January 1999.
- [71] Nigel T. Bishop. Linearized solutions of the Einstein equations within a Bondi Sachs framework, and implications for boundary conditions in numerical simulations. *Classical and Quantum Gravity*, 22(12):2393–2406, June 2005.
- [72] Casey J. Handmer and Béla Szilágyi. Spectral characteristic evolution: a new algorithm for gravitational wave propagation. *Classical and Quantum Gravity*, 32(2):025008, January 2015.
- [73] Casey J. Handmer, Béla Szilágyi, and Jeffrey Winicour. Gauge invariant spectral Cauchy characteristic extraction. *Classical and Quantum Gravity*, 32(23):235018, December 2015.
- [74] Nigel T. Bishop and Luciano Rezzolla. Extraction of gravitational waves in numerical relativity. *Living Reviews in Relativity*, 19(1):2, October 2016.
- [75] Tony Chu, Heather Fong, Prayush Kumar, Harald P. Pfeiffer, Michael Boyle, Daniel A.

- Hemberger, Lawrence E. Kidder, Mark A. Scheel, and Bela Szilagyi. On the accuracy and precision of numerical waveforms: effect of waveform extraction methodology. *Classical and Quantum Gravity*, 33(16):165001, August 2016.
- [76] Casey J. Handmer, Béla Szilágyi, and Jeffrey Winicour. Spectral Cauchy characteristic extraction of strain, news and gravitational radiation flux. *Classical and Quantum Gravity*, 33(22):225007, November 2016.
- [77] Kevin Barkett, Jordan Moxon, Mark A. Scheel, and Béla Szilágyi. Spectral Cauchy-characteristic extraction of the gravitational wave news function. *Phys. Rev. D*, 102(2):024004, July 2020.
- [78] Lawrence E. Kidder et al. SpECTRE: a task-based discontinuous Galerkin code for relativistic astrophysics. *J. Comput. Phys.*, 335:84–114, 2017.
- [79] Thomas W. Baumgarte and Stuart L. Shapiro. *Numerical Relativity: Solving Einstein's Equations on the Computer*. Cambridge University Press, 2010.
- [80] L. Rezzolla and O. Zanotti. *Relativistic Hydrodynamics*. Oxford University Press, September 2013.
- [81] Luis Antón, Olindo Zanotti, Juan A. Miralles, José M. Martí, José M. Ibáñez, José A. Font, and José A. Pons. Numerical 3+1 general relativistic magnetohydrodynamics: a local characteristic approach. *The Astrophysical Journal*, 637:296–312, January 2006.
- [82] Jose A. Font. Numerical hydrodynamics and magnetohydrodynamics in general relativity. *Living Rev. Rel.*, 11:7, 2008.
- [83] Lee Lindblom, Mark A. Scheel, Lawrence E. Kidder, Robert Owen, and Oliver Rinne. A New generalized harmonic evolution system. *Class. Quant. Grav.*, 23:S447–S462, 2006.
- [84] Yoonsoo Kim, Elias R. Most, William Throwe, Saul A. Teukolsky, and Nils Deppe. General relativistic force-free electrodynamics with a discontinuous Galerkin-finite difference hybrid method. *Phys. Rev. D*, 109(12):123019, 2024.
- [85] William H. Press, Saul A. Teukolsky, William T. Vetterling, and Brian P. Flannery. *Numerical Recipes 3rd Edition: The Art of Scientific Computing*. Cambridge University Press, sep 2007.
- [86] Thomas W. Baumgarte and Stuart L. Shapiro. *Numerical Relativity: Solving Einstein's Equations on the Computer*. Cambridge University Press, 2010.
- [87] Rezzolla, L. and Zanotti, O. *Relativistic Hydrodynamics*. Oxford University Press, sep 2013.
- [88] Bram Van Leer. Towards the ultimate conservative difference scheme. iv. a new approach to numerical convection. *Journal of Computational Physics*, 23(3):276 – 299, 1977.
- [89] Heinz-Otto Kreiss. Methods for the approximate solution of time dependent problems. volume 10 of *Global Atmospheric Research Programme*. International Council of Scientific Unions, World Meteorological Organization, 1973.
- [90] Nils Deppe, Lawrence E. Kidder, Saul A. Teukolsky, Marceline S. Bonilla, François Hébert, Yoonsoo Kim, Mark A. Scheel, William Throwe, and Nils L. Vu. A positivity-preserving adaptive-order finite-difference scheme for GRMHD. *Class. Quant. Grav.*, 40(24):245014, 2023.
- [91] Saul A. Teukolsky. Formulation of discontinuous Galerkin methods for relativistic astrophysics. *J. Comput. Phys.*, 312:333–356, 2016.
- [92] L. Del Zanna, O. Zanotti, N. Bucciantini, and P. Londrillo. ECHO: an Eulerian conservative high order scheme for general relativistic magnetohydrodynamics and magnetodynamics. *Astron. Astrophys.*, 473:11–30, 2007.
- [93] Elias R. Most, L. Jens Papenfort, and Luciano Rezzolla. Beyond second-order convergence in simulations of magnetized binary neutron stars with realistic microphysics. *Mon. Not. Roy. Astron. Soc.*, 490(3):3588–3600, 2019.
- [94] Mark A. Scheel, Harald P. Pfeiffer, Lee Lindblom, Lawrence E. Kidder, Oliver Rinne, and Saul A. Teukolsky. Solving Einstein's equations with dual coordinate frames. *Phys. Rev.*, D74:104006, 2006.
- [95] Yuxi Chen, Gábor Tóth, and Tamas I. Gombosi. A fifth-order finite difference scheme for hyperbolic equations on block-adaptive curvilinear grids. *Journal of Computational Physics*, 305:604–621, 2016.

- [96] Michael Dumbser, Olindo Zanotti, Raphaël Loubère, and Steven Diot. A posteriori subcell limiting of the discontinuous Galerkin finite element method for hyperbolic conservation laws. *Journal of Computational Physics*, 278:47 – 75, 2014.
- [97] Per-Olof Persson and Jaime Peraire. Sub-cell shock capturing for discontinuous Galerkin methods. In *44th AIAA Aerospace Sciences Meeting and Exhibit*. American Institute of Aeronautics and Astronautics, Inc., 2006.
- [98] H. P. Pfeiffer, L. E. Kidder, M. A. Scheel, and S. A. Teukolsky. A multidomain spectral method for solving elliptic equations. *Comput.Phys.Commun.*, 152:253–273, May 2003.
- [99] Francois Foucart, Lawrence E. Kidder, Harald P. Pfeiffer, and Saul A. Teukolsky. Initial data for black hole-neutron star binaries: A Flexible, high-accuracy spectral method. *Phys. Rev. D*, 77:124051, 2008.
- [100] R. Haas, C. D. Ott, B. Szilágyi, J. D. Kaplan, J. Lippuner, M. A. Scheel, K. Barkett, C. D. Muhlberger, T. Dietrich, M. D. Duez, F. Foucart, H. P. Pfeiffer, L. E. Kidder, and S. A. Teukolsky. Simulations of inspiraling and merging double neutron stars using the Spectral Einstein Code. *Phys.Rev.D*, D93(12):124062, April 2016.
- [101] Nils L. Fischer and Harald P. Pfeiffer. Unified discontinuous Galerkin scheme for a large class of elliptic equations. *Phys. Rev. D*, 105(2):024034, 2022.
- [102] Nils L. Vu et al. A scalable elliptic solver with task-based parallelism for the SpECTRE numerical relativity code. *Phys. Rev. D*, 105(8):084027, 2022.
- [103] Nils Deppe et al. Simulating magnetized neutron stars with discontinuous Galerkin methods. *Phys. Rev. D*, 105(12):123031, 2022.
- [104] Michael Dumbser, Manuel Castro, Carlos Parés, and Eleuterio F. Toro. ADER schemes on unstructured meshes for nonconservative hyperbolic systems: Applications to geophysical flows. *Computers & Fluids*, 38(9):1731 – 1748, 2009.
- [105] Walter Boscheri and Michael Dumbser. Arbitrary-Lagrangian–Eulerian discontinuous Galerkin schemes with a posteriori subcell finite volume limiting on moving unstructured meshes. *Journal of Computational Physics*, 346:449 – 479, 2017.
- [106] Olindo Zanotti, Francesco Fambri, and Michael Dumbser. Solving the relativistic magnetohydrodynamics equations with ADER discontinuous Galerkin methods, a posteriori subcell limiting and adaptive mesh refinement. *Mon. Not. Roy. Astron. Soc.*, 452(3):3010–3029, 2015.
- [107] Francesco Fambri, Michael Dumbser, Sven Köppel, Luciano Rezzolla, and Olindo Zanotti. ADER discontinuous Galerkin schemes for general-relativistic ideal magnetohydrodynamics. *Mon. Not. Roy. Astron. Soc.*, 477(4):4543–4564, 2018.
- [108] G Dal Maso, P. G LeFloch, and F Murat. Definition and weak stability of nonconservative products. *Journal de mathématiques pures et appliquées*, 74(6):483–548, 1995.
- [109] Michael Dumbser and Dinshaw S. Balsara. A new efficient formulation of the hllm riemann solver for general conservative and non-conservative hyperbolic systems. *Journal of Computational Physics*, 304:275 – 319, 2016.
- [110] Michael Dumbser, Federico Guercilena, Sven Köppel, Luciano Rezzolla, and Olindo Zanotti. Conformal and covariant Z4 formulation of the Einstein equations: strongly hyperbolic first-order reduction and solution with discontinuous Galerkin schemes. *Phys. Rev.*, D97(8):084053, 2018.
- [111] Michael Dumbser, Francesco Fambri, Maurizio Tavelli, Michael Bader, and Tobias Weinzierl. Efficient implementation of ADER discontinuous Galerkin schemes for a scalable hyperbolic PDE engine. *arXiv e-prints*, page arXiv:1808.03788, August 2018.
- [112] Alvin Bayliss and Eli Turkel. Radiation boundary conditions for wave-like equations. *Communications on Pure and Applied Mathematics*, 33(6):707–725, 1980.
- [113] Oliver Rinne, Lee Lindblom, and Mark A. Scheel. Testing outer boundary treatments for the Einstein equations. *Class. Quant. Grav.*, 24:4053–4078, 2007.
- [114] Morten Bjørhus. The ode formulation of hyperbolic pdes discretized by the spectral collocation

- method. *SIAM Journal on Scientific Computing*, 16(3):542–557, 1995.
- [115] Sizheng Ma et al. Fully relativistic three-dimensional Cauchy-characteristic matching for physical degrees of freedom. *Phys. Rev. D*, 109(12):124027, 2024.
- [116] Amiram Harten, Peter D. Lax, and Bram van Leer. On Upstream Differencing and Godunov-Type Schemes for Hyperbolic Conservation Laws. *SIAM Review*, 25:35, 1983.
- [117] Richard C. Tolman. Static solutions of Einstein’s field equations for spheres of fluid. *Phys. Rev.*, 55:364–373, 1939.
- [118] J. R. Oppenheimer and G. M. Volkoff. On massive neutron cores. *Phys. Rev.*, 55:374–381, 1939.
- [119] José A. Font, Tom Goodale, Sai Iyer, Mark Miller, Luciano Rezzolla, Edward Seidel, Nikolaos Stergioulas, Wai-Mo Suen, and Malcolm Tobias. Three-dimensional numerical general relativistic hydrodynamics. II. Long-term dynamics of single relativistic stars. *Phys. Rev. D*, 65(8):084024, April 2002.
- [120] Gregory B. Cook, Stuart L. Shapiro, and Saul A. Teukolsky. Spin-up of a rapidly rotating star by angular momentum loss: Effects of general relativity. *The Astrophysical Journal*, 398:203, October 1992.
- [121] Gregory B. Cook, Stuart L. Shapiro, and Saul A. Teukolsky. Rapidly rotating neutron stars in general relativity: Realistic equations of state. *The Astrophysical Journal*, 424:823, April 1994.
- [122] F. Foucart, M. B. Deaton, M. D. Duez, L. E. Kidder, I. MacDonald, C. D. Ott, H. P. Pfeiffer, M. A. Scheel, B. Szilágyi, and S. A. Teukolsky. Black hole-neutron star mergers at realistic mass ratios: Equation of state and spin orientation effects. *Phys.Rev.D*, 87:084006, March 2013.
- [123] Xu-Dong Liu, Stanley Osher, and Tony Chan. Weighted essentially non-oscillatory schemes. *Journal of Comp. Phys.*, 115(1):200 – 212, 1994.
- [124] Guang-Shan Jiang and Chi-Wang Shu. Efficient implementation of weighted eno schemes. *Journal of Comp. Phys.*, 126(1):202 – 228, 1996.
- [125] R. Borges, M. Carmona, B. Costa, and W. S. Don. An improved weighted essentially non-oscillatory scheme for hyperbolic conservation laws. *Journal of Comp.Phys.*, 227(6):3191 – 3211, 2008.
- [126] Francis Bashforth and John Couch Adams. *An attempt to test the theories of capillary action by comparing the theoretical and measured forms of drops of fluid*. Cambridge University Press, 1883.
- [127] C. D. Muhlberger, F. H. Nouri, M. D. Duez, F. Foucart, L. E. Kidder, C. D. Ott, M. A. Scheel, B. Szilágyi, and S. A. Teukolsky. Magnetic effects on the low- $T/|W|$ instability in differentially rotating neutron stars. *Phys.Rev.D*, 90(10):104014, November 2014.
- [128] William Throwe and Saul Teukolsky. A high-order, conservative integrator with local time-stepping. *SIAM Journal on Scientific Computing*, 42(6):A3730–A3760, 2020.
- [129] Mike Boyle, Dante Iozzo, and Leo C. Stein. `moble/scri`: v1.2, September 2020.
- [130] Michael Boyle. Transformations of asymptotic gravitational-wave data. *Phys. Rev. D*, 93:084031, Apr 2016.
- [131] Michael Boyle, Lawrence E. Kidder, Serguei Ossokine, and Harald P. Pfeiffer. Gravitational-wave modes from precessing black-hole binaries. 9 2014.
- [132] Michael Boyle. Angular velocity of gravitational radiation from precessing binaries and the corotating frame. *Phys. Rev. D*, 87:104006, May 2013.
- [133] Michael Boyle and Mark Scheel. The `sxs` package, March 2024.
- [134] Xinghui Zhong and Chi-Wang Shu. A simple weighted essentially nonoscillatory limiter for Runge–Kutta discontinuous Galerkin methods. *Journal of Computational Physics*, 232(1):397 – 415, 2013.
- [135] J. Zhu, X. Zhong, C.-W. Shu, and J. Qiu. Runge-Kutta discontinuous Galerkin method with a simple and compact Hermite WENO limiter. *Communications in Computational Physics*, 19:944–969, April 2016.
- [136] P. Londrillo and L. Del Zanna. On the divergence-free condition in godunov-type schemes for

- ideal magnetohydrodynamics: the upwind constrained transport method. *J. Comput. Phys.*, 195:17–48, 2004.
- [137] Thomas A. Gardiner and James M. Stone. An Unsplit Godunov Method for Ideal MHD via Constrained Transport in Three Dimensions. *J. Comput. Phys.*, 227:4123–4141, 2008.
- [138] Andrew J. Cunningham, Adam Frank, Peggy Varniere, Sorin Mitran, and Thomas W. Jones. Simulating Magnetohydrodynamical Flow with Constrained Transport and Adaptive Mesh Refinement: Algorithms & Tests of the AstroBEAR Code. *Astrophys. J. Suppl.*, 182:519–542, 2009.
- [139] Francesco Miniati and Daniel F. Martin. Constrained-Transport Magnetohydrodynamics with Adaptive-Mesh-Refinement in CHARM. *Astrophys. J. Suppl.*, 195:5, 2011.
- [140] A. Mignone, C. Zanni, P. Tzeferacos, B. van Straalen, P. Colella, and G. Bodo. The PLUTO Code for Adaptive Mesh Computations in Astrophysical Fluid Dynamics. *Astrophys. J. Suppl.*, 198:7, 2012.
- [141] Dongwook Lee. A Solution Accurate, Efficient and Stable Unsplit Staggered Mesh Scheme for Three Dimensional Magnetohydrodynamics. *J. Comput. Phys.*, 243:269–292, 2013.
- [142] Dinshaw S. Balsara. Higher Order Accurate Space-Time Schemes for Computational Astrophysics – Part I – Finite Volume Methods. *Living Reviews in Computational Astrophysics*, 3(1):2, December 2017.
- [143] Andrea Mignone and Luca Del Zanna. Systematic construction of upwind constrained transport schemes for MHD. *J. Comput. Phys.*, 424:109748, 2021.
- [144] Kenta Kiuchi, Loren E. Held, Yuichiro Sekiguchi, and Masaru Shibata. Implementation of advanced Riemann solvers in a neutrino-radiation magnetohydrodynamics code in numerical relativity and its application to a binary neutron star merger. *Phys. Rev. D*, 106(12):124041, 2022.
- [145] Jeongbhin Seo and Dongsu Ryu. HOW-MHD: A High-order WENO-based Magnetohydrodynamic Code with a High-order Constrained Transport Algorithm for Astrophysical Applications. *Astrophys. J.*, 953(1):39, 2023.
- [146] Vittoria Berta, Andrea Mignone, Matteo Bugli, and Giancarlo Mattia. A 4th-order accurate finite volume method for ideal classical and special relativistic MHD based on pointwise reconstructions. *J. Comput. Phys.*, 499:112701, 2024.
- [147] Kevin Schaal, Andreas Bauer, Praveen Chandrashekar, Rüdiger Pakmor, Christian Klingenberg, and Volker Springel. Astrophysical hydrodynamics with a high-order discontinuous Galerkin scheme and adaptive mesh refinement. *Mon. Not. Roy. Astron. Soc.*, 453(4):4278–4300, 2015.
- [148] Laxmikant Kale, Bilge Acun, Seonmyeong Bak, Aaron Becker, Milind Bhandarkar, Nitin Bhat, Abhinav Bhatele, Eric Bohm, Cyril Bordage, Robert Brunner, Ronak Buch, Sayantan Chakravorty, Kavitha Chandrasekar, Jaemin Choi, Michael Denardo, Jayant DeSouza, Matthias Diener, Harshit Dokania, Isaac Dooley, Wayne Fenton, Juan Galvez, Filippo Gioachin, Abhishek Gupta, Gagan Gupta, Manish Gupta, Attila Gursoy, Vipul Harsh, Fang Hu, Chao Huang, Narain Jagathesan, Nikhil Jain, Pritish Jetley, Prateek Jindal, Raghavendra Kanakagiri, Greg Koenig, Sanjeev Krishnan, Sameer Kumar, David Kunzman, Michael Lang, Akhil Langer, Orion Lawlor, Chee Wai Lee, Jonathan Lifflander, Karthik Mahesh, Celso Mendes, Harshitha Menon, Chao Mei, Esteban Meneses, Eric Mikida, Phil Miller, Ryan Mokus, Venkatasubrahmanian Narayanan, Xiang Ni, Kevin Nomura, Sameer Paranjpye, Parthasarathy Ramachandran, Balkrishna Ramkumar, Evan Ramos, Michael Robson, Neelam Saboo, Vikram Saletore, Osman Sarood, Karthik Senthil, Nimish Shah, Wennie Shu, Amitabh B. Sinha, Yanhua Sun, Zehra Sura, Ehsan Totoni, Krishnan Varadarajan, Ramprasad Venkataraman, Jackie Wang, Lukasz Wesolowski, Sam White, Terry Wilmarth, Jeff Wright, Joshua Yelon, and Gengbin Zheng. Uiuc-ppl/charm: Charm++ version 6.10.2, August 2020.
- [149] J. D. Hunter. Matplotlib: A 2d graphics environment. *Computing in Science & Engineering*, 9(3):90–95, 2007.
- [150] Thomas A Caswell, Michael Droettboom, Antony Lee, John Hunter, Eric Firing, Elliott Sales

- de Andrade, Tim Hoffmann, David Stansby, Jody Klymak, Nelle Varoquaux, Jens Hedegaard Nielsen, Benjamin Root, Ryan May, Phil Elson, Darren Dale, Jae-Joon Lee, Jouni K. Seppänen, Damon McDougall, Andrew Straw, Paul Hobson, Christoph Gohlke, Tony S Yu, Eric Ma, Adrien F. Vincent, Steven Silvester, Charlie Moad, Nikita Kniazev, hannah, Elan Ernest, and Paul Ivanov. `matplotlib/matplotlib`: Rel: v3.3.0, July 2020.
- [151] T. Tantau. The `tikz` and `pgf` packages.
- [152] Utkarsh Ayachit. *The ParaView Guide: A Parallel Visualization Application*. Kitware, Inc., Clifton Park, NY, USA, 2015.
- [153] J. Ahrens, Berk Geveci, and C. Law. Paraview: An end-user tool for large-data visualization. In *The Visualization Handbook*, 2005.